

On the injection of helicity by shearing motion of fluxes in relation to Flares and CMEs

P. Vemareddy¹, A. Ambastha¹, R. A. Maurya² and J. Chae²

¹*Udaipur Solar Observatory, Physical Research Laboratory, Udaipur-313 001, India.*

²*Astronomy Program, Department of Physics and Astronomy, Seoul National University, Seoul 151-747, Korea*

vema@prl.res.in, ambastha@prl.res.in, ramajor@astro.snu.ac.kr,
jcchae@snu.ac.kr

ABSTRACT

An investigation of helicity injection by photospheric shear motions is carried out for two active regions (ARs), NOAA 11158 and 11166, using line-of-sight magnetic field observations obtained from the Helioseismic and Magnetic Imager on-board Solar Dynamics Observatory. We derived the horizontal velocities in the active regions from the Differential Affine Velocity Estimator (DAVE) technique. Persistent strong shear motions at the maximum velocities in the range of 0.6–0.9 km/s along the magnetic polarity inversion line and outward flows from the peripheral regions of the sunspots were observed in the two active regions. The helicities injected in NOAA 11158 and 11166 during their six days' evolution period were estimated as $14.16 \times 10^{42} \text{Mx}^2$ and $9.5 \times 10^{42} \text{Mx}^2$, respectively. The estimated injection rates decreased up to 13% by increasing the time interval between the magnetograms from 12 min to 36 min, and increased up to 9% by decreasing the DAVE window size from 21×18 to 9×6 pixel², resulting in 10% variation in the accumulated helicity. In both ARs, the flare prone regions (R2) had inhomogeneous helicity flux distribution with mixed helicities of both signs and that of CME prone regions had almost homogeneous distribution of helicity flux dominated by single sign. The temporal profiles of helicity injection showed impulsive variations during some flares/CMEs due to negative helicity injection into the dominant region of positive helicity flux. A quantitative analysis reveals a marginally significant association of helicity flux with CMEs but not flares in AR 11158, while for the AR 11166, we found marginally significant association of helicity flux with flares but not CMEs, providing evidences of the role of helicity injection at localized sites of the events. These short-term variations of helicity flux are further discussed in view of possible flare-related effects. This

study suggests that flux motions and spatial distribution of helicity injection are important to understand the complex nature of magnetic flux system of the active region leading to conditions favorable for eruptive events.

Subject headings: Sun: activity — Sun: flares — Sun: magnetic fields— Sun: Coronal Mass ejections— Sun: helicity injection

1. Introduction

Magnetic helicity is an important topological property of solar active regions (ARs) and is a measure of twist and writhe of the field lines (Berger & Field 1984; Finn & Antonsen 1985). It is gauge invariant for a closed volume of space. The Sun’s outer atmosphere is dominated by magnetic field at all scales. Dynamic phenomena, such as, energetic flares and coronal mass ejections (CMEs) occur due to the loss of equilibrium during the evolution of magnetic fields in solar ARs. Magnetic helicity has become an important physical parameter in the context of solar transient phenomena. It is one of the few global quantities which is conserved even in resistive magneto-hydrodynamics on a timescale less than that of the global diffusion. There exists no absolute measure of helicity within a sub-volume of space if that sub-volume is not bounded by a magnetic surface. However, a topologically meaningful and gauge invariant relative helicity for such volumes can be defined.

There are several methods for estimating helicity in solar ARs. By the force-free field assumption of coronal magnetic field, we have:

$$\nabla \cdot \mathbf{B} = \alpha \mathbf{B} \quad (1)$$

where α is the force-free parameter, also known as helicity or twist parameter. Assuming α to be constant for the whole AR, we can fit observed vector magnetograms to deduce the value of α (Pevtsov et al. 1995; Hagyard & Pevtsov 1999; Tiwari et al. 2009). Latitudinal variation of helicity of photospheric magnetic fields, and statistical significance of the observed temporal variations of the ARs’ hemispheric helicity rule, as measured by the latitudinal gradient of the best-fit linear force-free parameter α , etc., have been discussed by Pevtsov et al. (2008).

The Poynting-like theorem for helicity in an open volume as derived by Berger & Field (1984) is given by:

$$\frac{dH}{dt} = \oint 2(\mathbf{B}_t \cdot \mathbf{A}_p)v_z ds - \oint 2(\mathbf{A}_p \cdot \mathbf{v})B_z ds \quad (2)$$

where \mathbf{A}_p is the vector potential of the potential magnetic field, \mathbf{B}_p , which is uniquely specified by the observed flux distribution on the surface(x-y plane) as

$$\nabla \times \mathbf{A}_p \cdot \hat{z} = B_z; \quad \nabla \cdot \mathbf{A}_p = 0; \quad \mathbf{A}_p \cdot \hat{z} = 0 \quad (3)$$

where \hat{z} refers to unit vector along vertical direction of Cartesian-geometry. Equation 2 shows that the helicity of magnetic fields in an open volume may change by the passage of helical field lines through the surface (first term) and/or by photospheric footpoint motions of the field lines (second term). The temporal evolution of magnetic helicity flux across the photosphere characterizes the injection of magnetic helicity from the sub-photospheric layers into the solar atmosphere, horizontal flux motions, and the changes in the coronal magnetic field configurations related to eruptive events, such as the CMEs, propagating into the interplanetary medium.

During the past years, several attempts have been made to estimate magnetic helicity from suitable solar observations. [Chae \(2001\)](#) developed a method for determining the helicity flux (the second term in Equation 2) passing through the photosphere. They used a time series of photospheric line-of-sight (LOS) magnetograms to determine horizontal velocities by local correlation tracking (LCT) technique ([November & Simon 1988](#)). Using this method, vector potential \mathbf{A}_p was constructed by using photospheric LOS field (as an approximation to B_z field) as boundary conditions with Coulomb gauge in terms of Fourier Transform (FT) as:

$$\begin{aligned} A_{p,x} &= FT^{-1} \left[\frac{jk_y}{k_x^2 + k_y^2} FT(B_z) \right] \\ A_{p,y} &= FT^{-1} \left[\frac{-jk_x}{k_x^2 + k_y^2} FT(B_z) \right] \end{aligned}$$

where k_x, k_y are spatial frequencies in the x, y directions, respectively. Later, this method was applied to many ARs by several authors ([Chae et al. 2001](#); [Moon et al. 2002](#); [Nindos et al. 2003](#); [Chae et al. 2004](#)). However, [Pariat et al. \(2005\)](#) showed that this method of calculation introduced artificial polarities of both signs in the helicity flux density maps with many flow patterns. Therefore, they suggested to use relative velocities for calculating the helicity injection rate:

$$\frac{dH}{dt} = \frac{-1}{2\pi} \int_S \int_{S'} \frac{[(\mathbf{x} - \mathbf{x}') \times (\mathbf{u} - \mathbf{u}')]_n}{|\mathbf{x} - \mathbf{x}'|^2} B'_z(\mathbf{x}') B_z(\mathbf{x}) dS' dS \quad (4)$$

where \mathbf{u} is the foot-point velocity at the position vector \mathbf{x} , and B_z is the vertical component of the observed magnetic field. This equation shows that the helicity injection rate can be

understood as the summation of relative rotation rates of all the pairs of elementary fluxes weighted with their magnetic flux.

Furthermore, [Schuck \(2005\)](#) has shown that the LCT method is inconsistent with the magnetic induction equation, which governs the temporal evolution of the photospheric magnetic fields. Tracking methods have serious practical limitations that might result in the failure of detecting significant shear velocity fields and hence in the underestimate of the amount of helicity injected by such velocity fields. [Démoulin & Berger \(2003\)](#) reported that the magnetic energy and helicity fluxes should be computed only from the horizontal motions deduced by tracking the photospheric cross-section of magnetic flux tubes. These authors contend that the apparent horizontal motions include the effect of both the emergence and the shearing motions. They analyzed the observational difficulties involved in deriving such fluxes and in particular, the limitations of the correlation tracking methods. One of the main limitations in the previous studies has been the coarse spatial resolution of the available observations which limits the deduced velocities to the velocity corresponding to the group motion of an unresolved bunch of thin flux tubes covered by a pixel. Also, tracking motions faced difficulties in the areas lacking sufficient contrast, such as in the sunspot umbrae.

Several alternative, improved methods have been developed for inferring plasma velocities consistent with the induction equation at the photospheric level, based on the LOS, as well as, vector magnetograms. The Induction method (IM; [Kusano et al. 2002](#)), induction local correlation tracking (ILCT; [Welsch et al. 2004](#)), minimum energy fit (MEF; [Longcope 2004](#)), differential affine velocity estimator (DAVE; [Schuck 2005, 2006](#)) and differential affine velocity estimator for vector magnetograms (DAVE4VM; [Schuck 2008](#)) have been developed for the determination of horizontal component of motion. In contrast, the normal component of velocity can be determined from the doppler observations of ARs located near the disk center. DAVE4VM method requires vector magnetograms. The performance of different techniques has been examined in [Welsch et al. \(2007\)](#) which showed that the MEF, DAVE, FLCT, IM, and ILCT algorithms performed comparably. Furthermore, they reported that while the DAVE estimated the magnitude and direction of velocities slightly more accurately than the other methods, MEF's estimates of the fluxes of magnetic energy and helicity were more accurate.

Time series data of photospheric magnetograms have been extensively used to derive magnetic helicity and its evolution in order to examine its role in the level of transient activity of the ARs. [Moon et al. \(2002\)](#) reported impulsive variations of helicity during some M and X-class flares. In a survey, [LaBonte et al. \(2007\)](#) revealed that X-flaring ARs have a higher net helicity change with peak helicity rate $> 6 \times 10^{36} \text{Mx}^2 \text{s}^{-1}$ with weak hemispheric preference. [Park et al. \(2010b\)](#) have also studied the solar flare productivity in

relation to the helicity injection using a large sample of 378 active regions. Using SOHO-MDI magnetograms, they reported variation of helicity injection rates and a significant helicity accumulation of $(3 - 45 \times 10^{42}) \text{ Mx}^2$ over several days around the time of flares above M5.0. Most of the previous studies that used data from Michelson Doppler Imager (MDI) onboard SOHO had the time resolution of 96 minutes. The rather coarse time resolution between two consecutive observations has been a matter of concern in the above calculations because the contribution from the motion of short lived magnetic features in small intervals is difficult to be accounted suitably (*e.g.*, [Chae et al. 2004](#)). This underlines the need for observations of magnetic fields with higher temporal resolution.

The above mentioned issues can now be addressed with the availability of a better cadence of 12 minutes by the recently launched Helioseismic and Magnetic Imager (HMI) onboard *Solar Dynamics Observatory* (SDO). Our main objective in the present work is to reinvestigate the role of helicity injection in relation with flares and CMEs using the high-resolution data obtained from SDO-HMI. We intend to utilize this opportunity to revisit some of the previous studies involving computations of helicity rate for two ARs, NOAA 11158 and NOAA 11166, that appeared during February and March 2011, respectively, in the ascending phase of the current Solar Cycle 24.

Using the high quality HMI data obtained for the two ARs, we intend to examine whether the variations as reported by [Moon et al. \(2002\)](#) and [Park et al. \(2010a\)](#) for energetic flares occurred also during the flares of lower magnitude. It is of particular interest to investigate if such changes were associated with the CMEs as well. For our analysis, we use DAVE technique for retrieving horizontal foot-point velocity from the LOS magnetograms. Thereafter, using Equation 4 we determine helicity injection rates and the accumulated helicity in the two ARs due to foot-point shearing motions during their disk transit. It has been inferred from the previous studies that most of the helicity injection corresponds to magnetic flux emergence in the ARs([Jeong & Chae 2007](#)). We, therefore, attempt to interpret the variations found in these physical parameters in relation to the occurrence of flares and CMEs. In particular, we investigate whether the transport of magnetic helicity plays a role in solar eruptions.

We organize this paper as follows. Description of the data used in this study and the procedures of the data processing are given in Section 2. Results obtained for the two selected ARs are presented in Section 3 and the following discussions in Section 4. The summary of the work presented in this article is given in Section 5.

2. Data and Method of Analysis

For our study, we have used high resolution LOS magnetograms at a cadence of 12 minutes obtained from the Helioseismic Magnetic Imager (HMI; Schou et al. 2012) on board *Solar Dynamic Observatory* (SDO). HMI observes the full solar disk in the Fe I 6173Å spectral line with a spatial resolution of 1 arc-second. HMI provides four main types of data: dopplergrams (maps of solar surface LOS velocity), continuum filtergrams (broad-wavelength maps of the solar photosphere), LOS and vector magnetograms (maps of the photospheric magnetic field).

NOAA 11158 (19°S) and 11166 (10°N) appeared on the disk during February 11-20, 2011 and March 03-16 2011 respectively. These ARs were very active, and produced some intense X-class flares associated with CMEs in addition to many M- and C- class flares during their disk transits. From the AIA observations, intermittent mass expulsions were seen, many of which turned into large, fast moving CMEs as further confirmed by STEREO. Table 1 gives a list of flares¹ (as recorded by GOES) and CMEs².

Magnetograms obtained at different times were aligned by the method of Chae et al. (2004). In this method, an image of the AR taken at the central meridian is considered as the reference image. All other images, in time accounted for differential rotation (Howard et al. 1990) along with the latitudinal difference of center of reference image from the ephemeris information, were remapped on to the disk center. This method is intended to reduce errors due to geometrical foreshortening and the AR is transformed to the disk center. Since at disk center, normal and vertical components of magnetic fields are same, the difference between the normal and LOS component was corrected by cosine of the distance of the AR center from the disk center by assuming the horizontal field contribution for the transformation to be negligible (Venkatakrishnan & Gary 1989).

We followed the transits of the two selected ARs from east to west on the solar disk. In order to have negligible errors in geometric correction, we restricted ourselves to a region within $\pm 40^\circ$ longitude from the central meridian. With this constraint, we confined our study of the temporal evolution of the ARs to six days’s period around their central meridian passage.

We derived the horizontal velocities of foot-points on the photosphere by using DAVE technique (Schuck 2006). The DAVE technique is essentially a local optical flow method

¹Obtained from the website www.solarmonitor.org

²by scrutinizing AIA 304Å quicklook images mirrored at <http://jsoc.stanford.edu/data/aia/images/2011/> and further confirmed by the timings from <http://spaceweather.gmu.edu/seeds/>

Table 1: List of Flares and CMEs

AR (NOAA)	Date dd/mm/yyyy	Flares magnitude(time UT)	CMEs (time UT)
11158	11/02/2011	No flares	No CMEs
	12/02/2011	No flares	No CMEs
	13/02/2011	C1.1(12:29),C4.7(13:44),M6.6(17:28)	21:30,23:30
	14/02/2011	C1.6(02:35),C8.3(04:29),C7.1(06:51)	02:40,07:00,12:50,17:30,19:20
		C1.8(08:39),C1.7(11:51),C9.4(12:41)	
		C7.0(13:47),M2.2(17:20)*,C6.6(19:23)	
		C1.2(23:14), C2.7(23:40)	
	15/02/2011	X2.2(01:44),C2.7(00:31)	00:40,02:00*,03:00,04:30,05:00
		C4.8(04:27),C4.8(14:32),C1.7(18:07)	09:00
		C6.6(19:30),C1.3(22:49)	
16/02/2011	C2.0(00:58),C2.2(01:56),C5.9(05:40)	14:35	
	C2.2(06:18),C9.9(09:02),C3.2(10:25)		
	C1.0(11:58),M1.0(01:32),M1.1(07:35)		
	M1.6(14:19),C7.7(15:27),C1.3(19:29)		
	C1.1(20:11),C4.2(21:06),C2.8(23:02)		
11166	06/03/2011	C5.1(11:56),C3.9(15:21)	02:00,15:20
	07/03/2011	M1.9(13:45)	14:25,22:10
	08/03/2011	C7.7(23:10)	14:30,19:00
	09/03/2011	C9.4(08:23),M1.7(10:35),M1.7(13:17)	06:40,10:40,21:45
		C9.4*(22:03),X1.5(23:13)	
	10/03/2011	C2.9(03:50),C6.2(07:03),C4.2(13:19)	
		C4.7(13:42),C2.0(14:21)	04:50,07:10
		C4.0(19:00),M1.1(22:34)	
	11/03/2011	C1.4(00:29),C1.1(01:46),C2.8(02:24)	00:50
		C5.5(04:15),C4.3(07:22),C1.1(08:13)	
C2.0(11:10),C3.6(11:43),C1.1(16:04)			
C1.0(22:20),C1.0(22:50)			

Note: All flares(CMEs) associated to source region R2(R1) of respective ARs except those marked by *

that determines the magnetic footpoint velocities within the windowed region. Further, it adopts an affine velocity profile specifying velocity field in the windowed region about a point and constrains that profile to satisfy the induction equation. Any tracking method depends on two parameters, *viz.*, the window size and the time interval. For a given time interval Δt , the window should be large enough so that tracked features remain confined within the window. Also, it should be small enough to be consistent with an affine velocity profile. Schuck (2008) presented a way to select an optimal window objectively, using the degree of consistency between change in the observed magnetic field ($\Delta B/\Delta t$) and the expected magnetic field change based on the flow estimated with several trial windows. They found the best performance of this method at approximately a square window of pixels. Since the ARs evolved rapidly, we chose a window size of 21×18 pixel² after a careful verification of the physical flux motions and directions of estimated flows. The dependence of helicity injection rate on window size and time difference between the tracked maps using this method were investigated. Moreover, as the HMI magnetic field measurement precision is 10G (Schou et al. 2012), we have set this as the threshold to avoid errors while retrieving velocities. Further details of this method are given in a recent work of Tian et al. (2011).

Computation of the helicity rate using the method (direct integration) proposed by Pariat et al. (2005) at each pixel of the AR map (*cf.*, Equation 4) is a tedious, time consuming process. However, we chose to use this method for reducing the effect of fake polarities of helicity flux. Restricting the calculations at pixels with magnetic field above the threshold ($\geq 10\text{G}$) helps to reduce the computation time typically by 15-25%. Parallelization in integrand computation further reduces the time approximately by a factor of the number of processors used. The same equation as rewritten by Chae (2007) to suit the convolution algorithm by Fourier transform is faster than the direct integration method. The intrinsic problem of Fourier transform with periodicity could be overcome by padding the array corresponding to the data points with rows and columns of zeros to get results as obtained by direct integration method. In this study, we have implemented the former approach (direct integration) to get sufficiently accurate results.

3. Evolution of Magnetic Flux and Helicity

The evolution of observed magnetic flux and the computed helicity rates are presented in the following for the two selected ARs NOAA 11158 and NOAA 11166 with the methods and procedures explained in Section 2.

3.1. AR NOAA 11158

This AR appeared as small pores at the heliographic location E33S19 on 2011 February 11 as seen in the full disk HMI photoheliograms. Thereafter, it grew very rapidly during the next two days as the small pores merged and formed bigger sunspots. It was a newly emerging region which developed to a large AR having $\beta\gamma\delta$ magnetic complexity during its rapid evolution. It consisted of four large regions of opposite polarities in quadrupolar configuration. Figure 1(top row) shows the evolution of NOAA 11158 during 2011 February 13-15 in HMI intensity maps. The prominent positive polarity sunspots of the AR are labeled as SP1, SP2, SP3 and the negative polarity spots as SN1, SN2, SN3 for identification. LOS contours are overlaid on the intensity image showing the respective polarity distribution.

The spatial evolution of the AR shows a large shearing motion of SP2 that rotated around SN2 about its umbral axis during 2011 February 13-15. It then detached and moved towards SP3 along with small patches of both polarities appearing and disappearing over short periods of time. This motion appeared to have created a twist in magnetic fieldlines connecting these spots. A careful examination of the animation made from magnetograms and intensity maps revealed a significant counter clock-wise (CCW) rotation of SN1 during the same period, while a small positive polarity region SP1 located to the north of SN1 rotated in the counter clock-wise direction along with a proper motion away from SN1. The rotations of SN1 and SP1 increased the twist of the field lines, and the magnetic non-potentiality of the sigmoid structure (Canfield et al. 1999). Several mass expulsions were launched intermittently from this region, as seen from the quick look images in AIA. These turned into CMEs as confirmed by STEREO observations.

In order to quantitatively analyze the magnetic complexity or twist contributed by the observed shearing motions of the magnetic foot points, we computed the helicity injection rates using the temporal sequence of magnetograms of the AR. Figure 1(bottom row) shows the computed helicity flux density maps corresponding to the HMI continuum intensity images (top row). The dark (white) patches in the right panel represent negative (positive) helicity flux density according to the usual convention. Contours of LOS magnetic field at $[-150, 150]$ G levels are overlaid for a better visualization of helicity flux density with respect to the magnetic polarity. Evidently, negative polarity region of SN1 injected negative (dark) helicity during 2011 February 14-15 which is also consistent with its physical CCW rotation. In contrast, SP2, SN2 and SN3 injected positive (white) helicity along with negative (dark) helicity in some small patches. We expect that the nature of motions in these areas could have influenced the helicity pattern there.

The photospheric maps of helicity flux (and its injection rate) provides spatial information about the basic properties of a link between the activity and its sub-photospheric roots

as reflected by the flux emergence process. In a sample of four active regions, Jeong & Chae (2007) found that helicity was mostly injected while fluxes emerged in the AR, suggesting it to be the major source of helicity injection. The flux cancellation process, on the other hand, resulted in a loss of coronal magnetic helicity, or inverse helicity injection. We thus infer that the AR possessed two main sites, of unstable energy storage systems marked by the rectangular boxes R1 and R2 in Figure 1. These sites had distinctly different injection of helicity flux density corresponding to the flux (or foot-point) motions, polarities and activity.

In order to show the transient activity of the AR as it evolved, we have plotted the disk integrated GOES soft X-ray flux (1–8Å channel) during February 11–17 in Figure 2(top) where the start times of flares of NOAA 11158 are marked by arrows. After its birth, the AR gradually evolved during 2011 February 11–13 as evident from the monotonic increase of fluxes in both polarities corresponding to 3×10^{21} Mx (Figure 2, middle). Then followed a rapid phase of flux emergence (of 9×10^{21} Mx) during February 13–14 after which it reached a plateau. Also plotted is the flux imbalance, *i.e.*, the ratio of the net flux and absolute total flux in the AR. The dominance of negative flux during February 13–15, and thereafter of the positive flux, is evident. Flux variations occurred in the range of $(9.5\text{--}12.5) \times 10^{21}$ Mx with the imbalance within 10% over six days. A significant flux decrease in both polarities by $\sim 1 \times 10^{21}$ Mx occurred till the time of the X2.2 flare. We shall discuss more about flux changes during X-flares in Section 4. The unusual rotating sunspots along with the increased fluxes indicated emergence of highly twisted fluxes from the sub-photospheric region (Leka et al. 1996), and not resulting from the surface flows alone. Most of the flare and CME activity of this AR occurred only after February 13/12:00UT, indicating that the rapid flux emergence could have played important role in triggering the transients.

In Figure 2(bottom), we have plotted the time profile of helicity injection rate (dH/dt), which is the summation of helicity flux density over the AR. Also plotted is the accumulated helicity, *i.e.*, the integrated helicity change rate over time ($\Delta H = \int \frac{dH}{dt} \Delta t$). The total accumulated helicity is estimated as 14.16×10^{42} Mx² during the six day period of 2011 February 11–16, with the peak helicity rate of 31.54×10^{40} Mx²h⁻¹. The occurrence times of the CMEs associated with the AR are marked by arrows in this panel for reference. An impulsive variation of helicity injection rate due to injection of negative helicity is discernible during the X2.2 flare and the concomitant CME. The helicity injection rate decreased during the period February 14/11:00–February 15/13:00 UT, and increased thereafter till February 16 along with fluctuations in the range $2\text{--}4 \times 10^{40}$ Mx²h⁻¹. We notice a large dip of helicity injection around X2.2 flare with associated CMEs. We have smoothed the original time profile at 12 minute interval by a box car window of five data points (*i.e.*, 1 hour). Similar sudden dips in injection rates during other events can be further analyzed for examining their association.

Figure 3 shows transverse velocities in the rectangular sub-regions R1 (top row) and R2 (bottom row) of NOAA 11158 overlaid on the corresponding maps of helicity flux density during three flare events. Also overlaid are the contours of the LOS magnetic flux at $\pm 150\text{G}$ levels. Maximum rms velocities in the range of $0.6\text{--}0.9\text{ km s}^{-1}$ were found over the observed period in the AR. Spiral or vortex like velocity patterns are obviously related to the counter rotation of SN1 in Figure 3(b–c). A notable observation is that the sub-region R1 possessed negative helicity flux density distribution which is consistent with the chirality associated with the physically observed counter rotation of SN1 whereas R2 possessed mixed helicity flux dominated by positive helicity flux distribution. Because of the continued shearing motions at the interface of SP2 and SN2, the flow field vectors almost aligned with the polarity inversion line (PIL) as seen in panels (d–f). Interaction of fluxes with this shear motion can squeeze and converge the flux in both SP2 and SN2. We hypothesize that the field lines were stressed and twisted by this motion leading to the storage of free energy adequate to account for the release in the energetic X2.2 flare of February 15/01:44UT. As almost all flares (except M2.2 at 14/17:20) occurred in R2, we examined the spatial distribution of helicity flux before and after the flare events to know whether any sudden changes are found related to the occurrence of flare. During some events, we noticed negative patch of helicity flux in the regions of positive helicity flux. Especially, in the panels (e–g), a negative helicity flux distribution near the PIL during M6.6, C7.0, and X2.2 flares can be observed. There may be some concern about these flare-related changes, as it is known that during the impulsive phase of large flares, the spectral line profile itself may undergo some change affecting the magnetic (and velocity) field measurements.

Most of these flares occurred in R2 while the mass expulsions(or CMEs) were associated to R1. In order to relate helicity rate changes to these events, therefore, we have computed and plotted the total injected quantities for R1 and R2 in Figure 4(a-b). Injection of helicity in a region of dominant opposite sign can be understood as a sudden dip in the time profile plot. Of course, the corresponding spatial information is lost in the averaged quantity. The advantage of using localized analysis of selected sub-areas in the ARs is that it reduces complex variations occurring over a much larger area of the entire AR while showing only the variations occurring in the areas-of-interest. It also enhances the dips corresponding to the identified events (marked by the arrows). However, it is important to identify the location of individual event in order to correctly attribute a particular change of helicity rate to it. NOAA 11158 was essentially a positive helicity injecting region, while its sub-region R1 had a negative injection rate and accumulated quantity due to the presence of rotational motion. We expect that as the sunspots SN1 and SP1 rotated, the injection rate increased to a maximum of $-16 \times 10^{40}\text{Mx}^2\text{h}^{-1}$ on February 14/18:00UT. A total helicity accumulation of $-5.60 \times 10^{42}\text{Mx}^2$ occurred during the six day period in this region. Noticeably, a steep

accumulation occurred during Feb 14–15 along with many observed mass expulsions shown by arrows. This could be interpreted as shedding of excess helicity from the corona in the form of eruptive events. The steep accumulation of helicity by monotonic injection rate, therefore, is suggested to be a cause of expulsions. Accumulated helicity amounting to $14.44 \times 10^{42} \text{Mx}^2$ in sub-region R2 with steep accumulation observed from February 13 onwards, could be mostly associated with the observed large shear motion of SP2.

For a quantitative study of the association of short term variations in helicity rate to the flaring or CME, the following analysis is carried out. The absolute time difference of the helicity flux ($|\Delta(dH/dt)|$, having units same as dH/dt) averaged over start and stop times of GOES flares above C2.0 is computed. This is compared to that of randomly selected but equal length time intervals containing no flares. A significantly higher mean of $|\Delta(dH/dt)|$ during flares compared to quiet times would indicate a robust association between flaring and helicity fluxes. A similar analysis is undertaken for time windows around CMEs to look for a CME-helicity flux association. We assume that there is no time lag between flaring and helicity flux signal while carrying out this analysis. We first interpolated the signal at 1 min interval from 12 min interval to get values as required by the GOES flare times, then it was smoothed to a boxcar width of 30 minutes. Within start and stop times of flares, the averaged value of absolute variation was computed to compare with that calculated during randomly selected, constant interval(30 min) quiet times.

The time difference of helicity rate in R1-R2 is shown in Figure 4(c-d) with CMEs and flares marked by arrows. Large amplitude variations are discernible during M6.6, X2.2 and the CME at 12:30UT indicating some association, but similar variations are present around the mean position even in quiet times. From the above described analysis, we found a significantly higher mean during CME's (0.054 ± 0.007) compared to quiet times(0.032 ± 0.008). The difference in CME versus quiet time helicity fluctuations are marginally statistically significant, at better than one-sigma. Similarly, a mean of 0.044 ± 0.004 (0.049 ± 0.008) during flare (quiet) times indicate poor or no association of flaring to helicity flux variations. The same analysis for the helicity flux over the entire AR improved the association (in terms of mean absolute helicity variation) slightly for CMEs but worsened it for flaring. We shall further discuss these helicity variations during flare/CMEs in view of the involved flare-related effects in Section 3.3.

3.2. AR NOAA 11166

AR NOAA 11166 appeared on the east limb of solar disk on 2011 March 03 at the location N10E64. We monitored its activity during the period of 2011 March 6–11 in which

it produced a large X1.5 flare, two M-class flares and several C-class flares, some of which were also associated with plasmoid ejections or CMEs. Table 1 lists the flares and CMEs of this AR. Daily evolution of the AR in the period of March 8-11, 2011 is shown in Figure 5(top row).

The major sunspots of the AR are labeled as SP1, SP2, SN1 and SN2. The identification of SP2 was somewhat unclear before March 10 as several small umbrae were spread over its location. They moved and coalesced to form SP2. Polarities of the respective sunspots are identified by the overlaid LOS magnetic field contours. This AR also consisted of a complex magnetic configuration with two positive (SP1, SP2) and two negative (SN1, SN2) polarity sunspots located within the surrounding diffused fluxes. Emerging and moving flux regions, FP3 and FN2, were identified in the course of the evolution in the sunspot periphery (March 11/22:00UT panel), having opposite sign to that of their native sunspots. However, there were no intrinsic rotating sunspots or flux patches as observed in the case of AR NOAA 11158.

We computed the helicity flux density for AR NOAA 11166 during its evolution in the period 2011 March 6–11. The corresponding maps for three successive days are plotted in Figure 5(bottom row). Locations of helicity flux density of mixed sign were distributed all over the AR through out the evolution period. The peripheral sites of the sunspots exhibited helicity flux density predominantly of negative sign. However, patches of negative helicity flux were also observed embedded in the positive helicity flux site of the flare (March 09/23:00UT panel). For further close examination, we consider two sub-areas R1 and R2, as marked by the boxes in this panel.

The disk integrated GOES soft X-ray flux (1-8Å channel) during 2011 March 6-11 is plotted in Figure 6(top). The arrows in this panel indicate the start time of flares in NOAA 11166. During the disk transit of the AR, fluxes of both polarities increased corresponding to 5×10^{21} Mx, with the imbalance varying below 6% (Figure 6, middle). As observed for NOAA 11158, a rapid flux emergence occurred in this AR too during March 7–9. Thereafter, only small variations associated with local cancellations/emergence of about $\sim 1 \times 10^{21}$ Mx took place pertaining to the gradual evolution of the AR. Positive flux dominated in the AR during March 7-11, and then a near balance was established. It is worth noticing that magnetic fluxes in both polarities decreased by $\sim 0.9 \times 10^{21}$ Mx while evolution of fluxes leading to the occurrence of a CME following the X1.5 flare. However, it is not clear whether this decrease in flux six hours before the flare/CME has some role in these events. But, the flux imbalance, increasing prior to the flare, reduced significantly after the flare consistent with observations reported by Wang & Liu (2010). Most of the flares and CME activity of this AR occurred only after March 8, suggesting that the rapid emergence of fluxes could be an

important factor for triggering of these transients.

Temporal evolution of helicity injection rate and the accumulated helicity for NOAA 11166 are shown in Figure 6(bottom) with arrows marking the times of the CMEs. A five magnetogram boxcar was used to smooth the profile to reduce fluctuations in the profile. As expected, these parameters increased in the first phase corresponding to the flux emergence, in agreement with Jeong & Chae (2007) that helicity is mostly injected while the fluxes emerged. Total helicity accumulated during the six days' period of the AR's evolution was estimated to $\sim 9.5 \times 10^{42} \text{Mx}^2$. The maximum helicity injection occurred during 2011 March 8 at the rate of $30 \times 10^{40} \text{Mx}^2 \text{h}^{-1}$. Thereafter, it reduced gradually to the minimum rate at $-10 \times 10^{40} \text{Mx}^2 \text{h}^{-1}$ on 2011 March 10. The coronal helicity of the AR is likely to be positive as a result of this positive helicity injection.

Horizontal, or transverse, velocity vectors corresponding to the tracked flux motions are plotted in Figure 7 separately for R1 (top row) and R2(bottom row). The rms velocities of flux motions are found to have the maximum values in the range $0.5\text{--}0.9 \text{ km s}^{-1}$. Strong moat flows were systematically dominant in both regions from the peripheral regions of sunspots in addition to the shear flows. Persistent strong shear motions due to the merging SP2 group were identified in R2. These flows appear to collide head on with those from SP1 resulting in the flux submergence/cancellation. Flux emergence was also identified from the diverging flow field observed in animated flows from R1. From this region, flux moved towards R2 as the AR evolved. Such motions appear to be associated with injection of negative helicity into a region with predominantly positive flux, increasing the complexity of the magnetic flux system as shown in panels (d)–(f) of R2. Further, these negative helicity injections often coincided with some observed events, such as the three of them shown in this plot. For the X1.5 flare the distribution of helicity flux is shown in panel (e) on March 09/23:36UT.

The injection rates and accumulated helicities deduced from sub-regions R1 and R2 are plotted in Figure 8(a–b). Also the contribution of each signed helicity flux in the net helicity flux is plotted separately. The time profile of R1 shows it to have positive helicity injection with a steep increasing phase during March 7–9 at a peak rate of $27 \times 10^{40} \text{Mx}^2 \text{h}^{-1}$. Thereafter, gradual decrease in the rate of injection is evident from the plot. As mentioned earlier, R1 was a site of emerging flux that resulted in contributing to accumulation of helicity amounting to $11 \times 10^{42} \text{Mx}^2$. While R2 exhibited mixed sign injection rates during its evolution. As in the previous AR, continuous injection of dominant positive helicity from R1 is suggested to be the cause of observed mass expulsions, whereas the injection from R2 is of mixed signs suggested to result in flares. An enhanced peak of helicity rate was seen around the time of the X1.5 flare in R2 of AR 11166 that was not obvious in Figure 6(bottom

panel) since we reduced fluctuations occurring over entire AR by selecting small area. After this event, the negative injection rate increasingly dominated on March 10, turning the net injection of the entire AR negative. The implication of this transition of injection rate from positive to negative sign over a day is not clear in the observed events shown by the arrows.

The time variation of helicity flux in both R1 and R2 are plotted in Figure 8(c–d) along with the arrows pointing start times of CMEs and flares in the AR. Some of the large amplitude variations of helicity flux about the mean position appear to be related to these events. As in the previous AR, we have analyzed the association of flare/CMEs that originated from the sub-regions R1 and R2 of this AR with the respective helicity flux. The calculated mean of variation in helicity flux ($|\Delta(dH/dt)|$) during flaring (0.099 ± 0.020) is marginally statistically different at about two-sigma level over that during quiet times (0.057 ± 0.007), reflecting a robust association of flaring and helicity fluxes. The mean of $|\Delta(dH/dt)|$ obtained in quiet times do not have any information or bias of flaring or CME, therefore higher mean during the flare/CMEs implies some impact of helicity flux variations in them. A similar analysis undertaken for CMEs also showed the similar association(during CMEs of 0.052 ± 0.006 dominated over quiet times of 0.047 ± 0.006 , but not statistically significant difference). However, the association strengthened for flaring and weakened for CMEs when the helicity flux over the entire AR was considered in the analysis.

3.3. Flare-related effects on Helicity flux

It is well known that the photospheric magnetic (and Doppler) field measurements are affected by flares. During an energetic flare, the profile of spectral line used for the measurement was reported to change from absorption to emission, resulting in a change of sign in the deduced magnetic polarity (Qiu & Gary 2003, and references therein). This abnormal polarity reversal was observed to last for about a few minutes during the impulsive phase of the flare (typically 3-4 minutes). Similar abnormal, transient changes have also been reported for some other large, white light flares (Maurya & Ambastha 2009; Maurya et al. 2012). The change in the line profile may arise due to both thermal effects and non-thermal excitation and ionization by the penetrating electron jets produced during the large flares. We term these as flare-related transient changes, considered to be artifacts as they do not correspond to real magnetic field changes.

There is increasing evidence that flares may change the magnetic field more significantly on a persistent and permanent manner (Sudol & Harvey 2005; Petrie & Sudol 2010; Wang & Liu 2010). The persistence of the observed field changes implies that they are not artifacts of changes in the photospheric plasma parameters during the flare, and the tem-

poral and spatial coincidences between flare emission and the field changes suggest the link of the field changes to the flare. We term these as permanent flare-related changes. With these known transient and permanent flare-related effects on magnetic fields, it would not be clear, particularly during the impulsive phase of the flare, if the change in helicity flux can be interpreted as genuine transport of helicity across the photosphere.

In addition, an implicit assumption made in our approach of calculating helicity injection is the ideal evolution of photospheric magnetic fields in the induction equation used to derive velocities of flux motions. Moreover, the same assumption is involved in the derivation of helicity injection from the relative helicity formula (Berger & Field 1984; Finn & Antonsen 1985). This assumption is valid and reasonable outside the flaring time intervals (at least during permanent changes of fields) as the typical observed photospheric velocities are far less than the Alfvén velocities. In the real conditions of rapid, transient changes in photospheric magnetic fields spanning impulsive period of the flare, the assumption of ideal magnetic evolution may not be applicable. Therefore, there is theoretical uncertainty regarding the interpretation of helicity fluxes during flares.

In order to inspect these aspects in the signal of the helicity change rate, we procured 45s cadence magnetograms for some selected flare events and averaged them to 3min cadence after processing as the previous data set. A mosaic of distribution of helicity flux around the X2.2 flare is shown in Figure 9. During the impulsive period (01:48-02:02UT) of this flare, negative helicity flux is distributed about the PIL which we believe to be due to the transient flare-related effect. The magnetic (and Doppler) transients and locations of spectral line reversal associated with this flare are already reported by Maurya et al. (2012), which are spatially and temporally consistent with this negative helicity flux distribution. Therefore, the observed negative helicity flux distribution in the dominant positive site can be attributed to the transient flare-effect, and is likely to be artifact, i.e., not a true transfer of helicity.

Similar mosaics of helicity flux distribution maps were made and examined for other events. The computed magnetic and helicity fluxes are plotted with time in Figure 10. The flare start time is shown in vertical dotted line labeled with magnitude of the flare. It should be noted that we have not applied any smoothing to the computed helicity rate signal in these panels. Magnetic fluxes of both signs decreased abruptly with a dip during the impulsive period following with injection of negative helicity flux in the dominant positive helicity flux, during the M6.6, X2.2 flare events. Magnetic field measurements could also be underestimated by 18-25% due to enhanced core emission of spectral line by the heating of the impulsive flare (Abramenko & Baranovsky 2004) as a result of which the integrated flux profile could show such a dip during peak phase of the flare. Interpretation of flux

annihilation through reconnection during this peak phase might be ambiguous due to this fact, although it could be a possible consideration. In the post-flare phase, fluxes increased in both polarities as field lines reorganized as a post-reconnection process. This falls under the “permanent” real change related to the flare.

For smaller magnitude flares, transient effects may be absent or not be prominent in the impulsive phase. Therefore the measurements of magnetic fields and the computed helicity rate signal are not expected to be affected during the flare. Hence, they may indicate true transfer of helicity flux, except for the theoretical uncertainties as mentioned above. In the case of the 14 February/13:47UT (C7.0) flare, shown in panels (b1)-(b2), indeed the variation of helicity signal occurs without the variations in magnetic fluxes associated to the flare-related effects. This may be an example of true transfer of helicity of the flux system, but with the theoretical uncertainty in our approach.

There are no significant variations in magnetic and helicity fluxes corresponding to the 09 March/09:23UT (C9.4), and 10:35UT (M1.7) flares. Large amplitude fluctuations in both sign of helicity signals during the CME just before the 09 March/22:03UT (C9.4) flare are apparent in panels (e1)-(e2). We speculate that these fluctuations subsequently led to the initiation of the prominent CME that followed the 09 March/23:13UT (X1.5) flare an hour later. Similarly, the transient flare effects might be responsible for the abrupt changes in magnetic fluxes resulting in variations of helicity injection signal during the X1.5 flare (panels (e1)-(e2)). During the 10 March/13:19UT (C4.2), 13:42UT (C4.7) flares, the transfer of helicity flux from positive to negative, negative to positive sign is clear from the panels (f1)-(f2), respectively. These flares are of small magnitude, with no obvious flare-related artifacts. Therefore, the observed helicity flux changes are expected to be true (with the implicit theoretical uncertainty in the approach). A point to be noted is that all large flares (M and X-class) may be involved with transient flare effects. Therefore, it is better to look for helicity variations in small flares where magnetic fields are expected to be less affected, making it easier to examine the possible role of transfer of helicity flux. Thus, we consider the 14 February/13:47UT (C7.0), 10 March/13:19UT (C4.2) and 13:42UT (C4.7) flares to be the best examples here, supporting the true transfer of helicity. It is not clear that whether the helicity transfer in these cases is related to permanent flare-effects.

At present, it is difficult to say much about the physical significance of these variations over the AR in the corona, i.e., at the primary sites of the flares. It would be particularly interesting to study the physical significance of such injection along with the information of coronal connectivities (*e.g.*, [Chae et al. 2010](#)) as suggested by [Pariat et al. \(2005\)](#) for understanding the possible role of transfer of helicity flux during the flares/CMEs.

3.4. Dependence of Helicity Injection Rate on the DAVE Parameters

Computation of helicity injection rate involves the measurement of magnetic field and the inferred horizontal velocities. Apart from the errors in the measurements, the computations involving the DAVE method for deriving velocities depend on two main parameters *viz.*, the time interval between two successive magnetic maps, Δt , and the DAVE window size. For obtaining optimized results, horizontal displacements of features during the time interval Δt should be large enough to be well determined by DAVE. Also, these displacements should be smaller than the selected window size. To check our results for consistency, we carried out the DAVE calculations using the time intervals $\Delta t = 12, 24$ and 36 minutes, while keeping the window size fixed at 21×18 pixels. Then, calculations were carried out for different window sizes, *viz.*, $21 \times 18, 15 \times 12, 9 \times 6$ while keeping Δt fixed at 36 minutes. Furthermore, to avoid the effect arising from noise, we used a threshold of magnetic field at 10G , which is the HMI precision. As the HMI provides 12 minute averaged data products, we averaged them corresponding to our calculations at 24 (2 maps) and 36 (3 maps) minutes.

The dependence of helicity injection rates on time interval Δt is shown in Figure 11 (top row) for NOAA 11158. The scattered data are fitted by straight line in the least square sense. Due to the large volume of data, this computation is tedious and time consuming. Therefore, results are shown here only for NOAA 11158, but, we expect they are also valid for other ARs observed by the HMI. There is an additional issue of unequally spaced data points to be addressed in case, for example, we intend to plot the results for $\Delta t=36$ with $\Delta t = 24$ minutes. For such cases, we used a cubic spline interpolation (*cf.*, Press et al. 1992), to get corresponding abscissa values for the ordinate points or vice-versa. Essentially, this algorithm employs cubic polynomial between each pair of data points with the constraint that the second and first derivatives of that polynomial are same at the end points so that the resulting values are smooth. Table 2 lists the minimum and maximum values of helicity injection rates (dH/dt , in units of $10^{40}\text{Mx}^2\text{h}^{-1}$) and the accumulated helicity (ΔH , in units of 10^{42}Mx^2) for the computational runs carried out with various DAVE parameters as mentioned above.

It can be observed from the scatter plots that the helicity rates decreased slightly as the time interval Δt is increased from 12 min to 36 min. The fitted straight line deviates at a slope of 0.87 and 0.91 corresponding to $\Delta t = 12$ versus 24 and $\Delta t = 24$ versus 36 min indicating that helicity injection decreases by 13% and 9% respectively. This implies that short-lived features and their dynamics have considerable contribution to helicity rates. The helicity rates at intervals of 36min are lower by a factor of 21% than that at 12 min with worst correlation coefficient of 0.79 . These effects in turn reflected in the variation of accumulated helicity by 9% . This implies that averaging in time between $12\text{-}36$ min has

Table 2: Helicity injection rates and Accumulated helicities at different DAVE parameters

DAVE parameters		AR 11158		
Δt	Window size	dH/dt		ΔH
min	pixel ²	min	max	
12	21x18	-18.98	31.54	14.16
24	21x18	-7.48	27.27	13.09
36	21x18	-1.06	22.52	12.96
36	21x18	-1.06	22.52	12.96
36	15x12	-1.06	25.02	13.51
36	9x6	-1.28	26.8	14.22

Units of dH/dt are $10^{40}\text{Mx}^2\text{h}^{-1}$ and ΔH are 10^{42}Mx^2

significant effect on injected helicity rates up to 13% corresponding to 9% of variation in accumulated helicity.

The dependence of helicity injection rate on window size by keeping the time interval Δt fixed at 36 minutes is shown in Figure 11(bottom row). The slopes of 1.09 and 1.05 for the DAVE windows 21×18 versus 15×12 and 15×12 versus 9×6 respectively, show increasing trend of helicity rates with decreasing window size. Indeed, a scalable factor of 14% reduction of helicity rate is evident for windows 21×18 versus 9×6 . Accumulated helicity also showed this increased trend with decreased window size. A total variation of 10% is found, however, with the same trend of helicity injection rate profiles which is discernible in correlation coefficient with the plots. A maximum velocity of $1 \text{ km}\cdot\text{s}^{-1}$ during the time interval of 12 min corresponds to a plasma displacement of an arc-sec. Hence, for the window size of $4.5'' \times 3''$ ($9 \times 6 \text{ pixel}^2$), the issue of features overflowing out of the window should not pose problem.

These results are consistent with those reported by [Chae et al. \(2004, their Figure 7\)](#). They deduced and compared velocity and helicity rates by combinations of time difference between magnetograms and LCT window size. Their rms velocity values varied up to 0.6km/s at time interval of 5min. They found that smaller values of LCT parameters result in larger amplitude fluctuations of the rate of helicity, with variation within 10%. We, in our computations, found maximum rms velocities for 12min, 24min and 36min in the AR as 0.95, 0.85 and 0.8km/s respectively. However for the window sizes 21×18 , 15×12 and 9×6 , we obtained the rms velocities as 0.8, 0.9 and 1.5km/s respectively. These are higher by a factor of 2 compared to their values probably due to the higher resolution and sensitivity of HMI as against the coarser spatial resolution of MDI of $1.98''/\text{pixel}$. Nevertheless, the variation

in accumulated helicity found in our analysis is within 10%; consistent with their result.

We thus, found the measured helicity injection rate to depend on the time interval between the two successive magnetograms, i.e., the observational cadence. The selected window size also influenced the measured quantities. Our analysis suggests that it is better to use images averaged over up to 24 minutes with relatively small DAVE window size subjected to the overflow condition as mentioned above. These are important considerations to derive reasonable and meaningful results in addition to optimizing the computations involving large data-sets.

4. Discussions

Free energy storage and release are some of the most important problems in the eruption physics of the Sun. There are essentially two effects that can supply magnetic free energy and helicity from below the solar surface to the corona. Flux emergence is the process in which vertical motions carry magnetic fluxes through the photosphere. If the sub-surface fluxes emerging through the photosphere are already twisted, then it will contribute to the injection of helicity (*cf.*, the 1st term in Equation 2). Computation of this term requires the knowledge of the vertical component of velocity and the horizontal or transverse component of magnetic field. Flux motions in the form of rotation or proper motions are another process that may efficiently supply helicity injection (*cf.*, the 2nd term in Equation 2). The helicity injected by solar differential rotation is rather small, less than 10% of that contributed by the flux motions (Chae et al. 2004; Démoulin et al. 2002), and has only a much longer term effect on helicity accumulation (DeVore 2000).

Magnetic helicity is a physical quantity having a positive or negative sign, representing a right-handed or left-handed linkage of magnetic fluxes, respectively. This means that if positive and negative helicities co-exist in a single domain, magnetic reconnection can cancel magnetic helicity by merging magnetic flux systems of opposite helicities. Helicity densities are not gauge-invariant. It is only area-integrated relative helicity flux that is gauge-invariant. In order to define true helicity flux density, the coronal linkage needs to be provided (Pariat et al. 2005), so the helicity flux density inferred from tracking will not be precisely accurate. Our computations of magnetic helicity injection in both ARs revealed that the distribution of helicity flux is highly complicated in time and space. Even the sign of helicity flux often changed within the AR.

It has been suggested earlier by several workers that magnetic helicity must play an important role in flares as a substantial amount of helicity accumulation is found before

many events (Kusano et al. 1995; Kusano & Nishikawa 1996; Kusano et al. 2002). However, the correlation between various magnetic field parameters and the flare index of an AR is not high irrespective of the method used. This is an intrinsic problem for flare forecasting as the occurrence of a flare depends not only on the amount of magnetic energy stored in an AR, but also on how it is triggered. Thus, it appears that helicity accumulation might be a necessary, but insufficient condition for the flares requiring a trigger even if a magnetic system has enough non-potentiality. For instance, Kusano et al. (2003) suggested that coexistence of positive and negative helicities may be important for the onset of flares.

Careful three-dimensional simulations have been carried out by Linton et al. (2001) to explore the physics of flux tube interaction for the co-helicity (same sign) or counter-helicity (opposite sign). According to them, counter-helicity presented the most energetic type of slingshot interaction in which flux is annihilated and twist is canceled. In contrast, co-helicity exhibited very little interaction, and the flux tubes bounced off resulting in negligible magnetic energy release.

Magnetic helicity in the solar corona is closely related to the photospheric magnetic shear, which is usually defined as the extent of alignment of the transverse component of magnetic field along the neutral or polarity inversion line (PIL)(Ambastha et al. 1993). Based on this idea, Kusano et al. (2004) performed a numerical simulation by applying a slow footpoint motion. This motion can reverse the preloaded magnetic shear at the PIL resulting in a large scale eruption of the magnetic arcade through a series of two different kinds of magnetic reconnections. They proposed a model for solar flares in which magnetic reconnection converts oppositely sheared field into shear-free fields.

We interpret our observations according to the above observational and simulation aspects as follows. We have found flux interactions during the X-class flares and associated CMEs as seen in Figure 3 in the form of continued shearing motion of SP2 around SN2 in AR 11158. Similar motions are also associated with SP2 in AR 11166. In both ARs cases, the flare prone regions (R2) had inhomogeneous the helicity flux distribution with mixed helicities of both signs. Correspondingly, sudden impulsive peaks appeared in the profiles of helicity injection due to the injection of negative signed helicity during some flare events. These were also spatially correlated with the observed flares. Opposite helicity flux tubes can interact easily leading to reconnection, thereby unleashing explosive release of magnetic energy. Impulsive variations of the magnetic helicity injection rate associated with eruptive X- and M- class flares accompanied with CMEs were reported also by Moon et al. (2002). Recently, Park et al. (2010a) conjectured that the occurrence of the X3.4 flare on 2006 December 13 was involved with the positive helicity injection into an existing system of negative helicity. Further, a solar eruption triggered by the interaction of two opposite-helicity flux

systems (Chandra et al. 2010; Romano et al. 2011), and occurrence of flares in relation to spatial distribution of helicity flux density (Romano & Zuccarello 2011) were reported. The main drawback of these findings is that the time span between two magnetograms is more than the duration of the flare ($\geq 96\text{m}$), so the time rate of helicity could not be easily resolved at the onset time of the flare. Therefore, our results appear to be consistent with the reports of opposite helicity flux tubes reconnecting to trigger transient events.

However, it should be cautioned that we have not found such variations of helicity flux clearly in all flare/CME events. From a quantitative analysis, we found poor association of difference in helicity rate during flares to that of quiet times in AR NOAA 11158. This indicates such variations are not prominent or present during all flares. Moreover, statistically significant association of such impulsive variations was found during CMEs compared to quiet times. There are many possible reasons for this poor association; one of them is time duration of helicity flux change. We first interpolated the signal at 1 min interval from 12 min interval to get values as required by the GOES flare times. Then, it was smoothed to a boxcar-averaging window of 30 minutes to reduce fluctuations arising due to interpolation. Within start and stop times of flares, the averaged values of absolute variation were computed. Here, averaging might have diluted the original helicity variation, so comparison with the helicity variation during quiet times might not be valid. In any case, there is no better way to find appreciable variation in the helicity flux over background fluctuations to incorporate into the correlation analysis, unless individual events are monitored manually to get variation timings. Despite these difficulties, statistically significant association of helicity flux is found during flares, but dominant association that is not statistically significant during CMEs in the AR 11166 by following the same approach.

Further, there are concerns about the flare-related effects on magnetic field measurements resulting in misleading interpretation of helicity flux transfer, in addition to the theoretical uncertainty with the assumption of ideal magnetic field evolution in the approach. We therefore investigated this issue using 3 min interval time sequence magnetograms. We found transient flare effects resulting in spurious negative helicity flux distribution during the X2.2, M6.6, and X1.5 flare events. Also, we indeed observed the true transfer of helicity flux with variations of opposite sign helicity without such flare-related effects in small flares such as the C7.0 on 14 February, C4.2 at 13:19UT, C4.7 at 13:42UT on 10 March. The important point to note is that we found statistically significant association of helicity flux variations with flares/CMEs in above cases of ARs at zero time lags. Also these variations are clear during the flare events (see Figure 10) and not before their commencement. Therefore, it is difficult to suggest that these variations triggered the flares. A study with the information of fieldline connectivity from coronal observations may be expected to reveal the physical significance of the role of helicity transfer during these events.

Our computed helicity rates involving photospheric flux motions include the flux emergence term as explained by [Démoulin & Berger \(2003\)](#). By a simple geometrical argument, horizontal foot-point velocity (\mathbf{u} , here the DAVE velocity) can be written in terms of horizontal and vertical plasma velocities, \mathbf{v}_h , v_n , respectively:

$$\mathbf{u} = \mathbf{v}_h - \frac{v_n}{B_n} \mathbf{B}_h. \quad (5)$$

From this relation, it is not possible to infer as to which term, *viz.*, the flux emergence or flux motions, governs the level of activity of the ARs. To resolve this difficulty, we have plotted the integrated absolute flux and accumulated helicity computed over the ARs, as shown in [Figure 12](#).

Evidently, the accumulated helicity increased monotonically with the emergence of magnetic flux in the AR in its first phase (marked by the vertical dashed line for NOAA 11158). After this phase followed the next, the active phase, where an appreciable increase of helicity occurred with only small variation in the flux, *i.e.*, where little emergence of fluxes occurred. This rapid increase in helicity in the second phase could be interpreted as the dominant contribution of the flux motions. Intermittent mass expulsions in the form of CMEs transferred away the excess helicity. The extent of this transfer, however, is not clear from this plot, although one can make plausible conclusions from the timings of the flares and CMEs. The X-class flares with associated CMEs in both ARs occurred at a slowing phase of helicity accumulation by negative helicity injection. These facts add to the cases as reported by [Park et al. \(2010b\)](#).

Moreover, it can be inferred for AR 11158, that less than 25% of the total helicity flux accumulated with the emergence of the first 75% of the magnetic flux. Most of the helicity flux (from about $3 - 13 \times 10^{42} \text{Mx}^2$) was accompanied by very little flux emergence (about $3 \times 10^{21} \text{Mx}$ out of the $30 \times 10^{21} \text{Mx}$). Therefore, more than 75% of the helicity flux came with only 10% of the total magnetic flux. Similarly, the first 60% ($19.5 - 28.0 \times 10^{21} \text{Mx}$) of total magnetic flux was associated to less than 30% ($3 \times 10^{42} \text{Mx}^2$ of $9.5 \times 10^{42} \text{Mx}^2$) of the total helicity flux in AR 11166. This implies that more than 70% of total helicity flux was accompanied with less than 40% of total magnetic flux. These two cases are thus contrary to the findings of [Jeong & Chae \(2007\)](#) stating that most of the helicity flux occurs during flux emergence. Our study suggests that flux emergence may not always play a major role in accumulating helicity flux. It is also evident that although flux emergence is necessary but horizontal motions also played crucial and dominant role over emergence term in increasing the complexity of magnetic structures contributing to the helicity flux. Therefore, we suggest that the horizontal flux motions contributed further, in addition to the emergence term, in

creating more complex magnetic structures that caused the observed eruptive phenomena.

5. Summary

We have studied the evolution of magnetic fluxes, horizontal flux motions, helicity injection and their relationship with the eruptive transient events in two recent flare (CME) productive ARs, NOAA 11158 and NOAA 11166 of 2011 February and March, respectively. We have used high resolution, high cadence data provided by SDO-HMI for these ARs which were in their emerging and active phases. The emerging AR consisted of rotating sunspots with increasing flux indicating emergence of twisted flux from the sub-photospheric layers. This indicated the transfer of twist or helicity injection through the photosphere to the outer atmosphere.

We suggest that strong shear motions that include rotational and proper motions played significant role in most of the events in addition to the flux emergence. Such motions are crucial in twisting or shearing the magnetic field lines and for further flux interactions. AR NOAA 11158 consisted of a CME-prone site of rotating main sunspot along with emerging flux of opposite sign and moving magnetic feature. It also had a flare-prone site consisting of self-rotating sunspot(SP2) moving about a sunspot of opposite sign(SN2), leading to flux interaction. These motions are likely to form the sigmoidal structures, which are unstable, and more likely to produce eruptive events. A huge expulsion as CME on 2011 February 14/17:30UT occurred in the former site and a white light, energetic X2.2 flare on 2011 February 15/01:44UT occurred in the later site. The other case, AR NOAA 11166 was already in its active phase with further increasing content of flux as it evolved. Group motions of diffused fluxes merging to form a bigger sunspot manifested major shear motions in addition to outward flows from sunspot. A large CME on 2011 March 09/21:45UT, followed by an X1.5 flare, was one of the major events in this AR.

AR NOAA 11158 injected $14.16 \times 10^{42} \text{Mx}^2$ while AR NOAA 11166 injected $9.5 \times 10^{42} \text{Mx}^2$ helicity during the six days' period of their evolution. These are consistent with the previously reported order of helicity accumulation (*e.g.*, [Park et al. 2010b](#)). It appears that due to the presence of rotational motions, the former AR accumulated larger amount of helicity accounting for its greater activity in the form of flares and CMEs. It is also evident that flux emergence is necessary and their motions are crucial in additionally accounting for the accumulated amount of helicity to the emergence term. In both ARs, X-class flares with associated CMEs were observed in the decreasing phase of helicity accumulation by the injection of opposite helicity.

Apart from the instrumental and computational errors, the estimation of helicity injection rates are also affected by the choice of DAVE parameters used to track the motion of the fluxes. Helicity injection rates are found to decrease up to 13% by increasing the time interval between magnetograms from 12 to 36 min whereas an increasing trend upto 9% resulted by decreasing the window size from 21×18 to 9×6 pixel², with a total variation of 10% in the deduced value of accumulated helicity.

The time profile of helicity rate exhibited sudden sharp variations during some flare events due to injection of opposite helicity flux into the existing system of helicity flux. In both ARs, the flare prone regions (R2) had inhomogeneous helicity flux distribution with mixed helicities of both signs and that of CME prone regions had almost homogeneous distribution of helicity flux dominated by single sign. A quantitative analysis was carried out to show the association of these variations to the timings of flares/CMEs. For the AR 11158, we find a marginally significant association of helicity flux with CMEs but not flares, while for the AR 11166, we find marginally significant association of helicity flux with flares but not CMEs. Moreover, these variations of helicity flux may not reflect true transfer; there exists flare-related transient effects and theoretical uncertainties resulting to these variations. We believe the helicity transfer in the cases of C7.0 on 14 February, C4.2 at 13:19UT, C4.7 at 13:42UT on 10 March to be true, without flare-related transient effect but with theoretical uncertainty in the approach.

Therefore, to further strengthen the above evidences of true helicity transfer, it would be worthwhile to scrutinize more flare/CMEs cases using 3 min cadence magnetic observations, over a period of a day or so. This will enable one to find detectable changes in helicity flux signal during smaller magnitude flares with less transient-flare effects. Interpreting the physical significance of such variations using the information of coronal connectivities will be another important aspect to add further to the present knowledge of helicity physics. Our study reveals that the spatial information of helicity injection is a key factor to understand its role in the flares/CMEs.

The data have been used here courtesy of NASA/SDO and HMI science team. We thank Dr. Etienne Pariat for checking our helicity program with comments and suggestions. The author expresses his gratitude to Prof. P. Venkatakrishnan for some useful discussions on the concept of helicity. We thank an anonymous referee for carefully reading the manuscript and making valuable comments which led to improved clarity and readability of the manuscript.

We thank Mr.Jigar Raval and Mr.Anish Parwage for their help in running program on one of the nodes of 3TFLOP HPC cluster at PRL computer center.

REFERENCES

- Abramenko, V. I., & Baranovsky, E. A. 2004, *Sol. Phys.*, 220, 81 [16](#)
- Ambastha, A., Hagyard, M. J., & West, E. A. 1993, *Sol. Phys.*, 148, 277 [21](#)
- Berger, M. A., & Field, G. B. 1984, *J. Fluid Mech.*, 147, 133 [2](#), [16](#)
- Canfield, R. C., Hudson, H. S., & McKenzie, D. E. 1999, *Geophys. Res. Lett.*, 26, 627 [9](#)
- Chae, J. 2001, *ApJ*, 560, L95 [3](#)
- . 2007, *Advances in Space Research*, 39, 1700 [8](#)
- Chae, J., Goode, P. R., Ahn, K., Yurchysyn, V., Abramenko, V., Andic, A., Cao, W., & Park, Y. D. 2010, *ApJ*, 713, L6 [17](#)
- Chae, J., Moon, Y.-J., & Park, Y.-D. 2004, *Sol. Phys.*, 223, 39 [3](#), [5](#), [6](#), [19](#), [20](#)
- Chae, J., Wang, H., Qiu, J., Goode, P. R., Strous, L., & Yun, H. S. 2001, *ApJ*, 560, 476 [3](#)
- Chandra, R., Pariat, E., Schmieder, B., Mandrini, C. H., & Uddin, W. 2010, *Sol. Phys.*, 261, 127 [22](#)
- Démoulin, P., & Berger, M. A. 2003, *Sol. Phys.*, 215, 203 [4](#), [23](#)
- Démoulin, P., Mandrini, C. H., van Driel-Gesztelyi, L., & et al. 2002, *A&A*, 382, 650 [20](#)
- DeVore, C. R. 2000, *ApJ*, 539, 944 [20](#)
- Finn, J. M., & Antonsen, T. M. 1985, *Comments Plasma Phys. Controlled Fusion*, 9, 111 [2](#), [16](#)
- Hagyard, M. J., & Pevtsov, A. A. 1999, *Sol. Phys.*, 189, 25 [2](#)
- Howard, R. F., Harvey, J. W., & Forgach, S. 1990, *Sol. Phys.*, 130, 295 [6](#)
- Jeong, H., & Chae, J. 2007, *ApJ*, 671, 1022 [5](#), [10](#), [14](#), [23](#)
- Kusano, K., Maeshiro, T., Yokoyama, T., & Sakurai, T. 2002, *ApJ*, 577, 501 [4](#), [21](#)
- . 2004, *ApJ*, 610, 537 [21](#)
- Kusano, K., & Nishikawa, K. 1996, *ApJ*, 461, 415 [21](#)
- Kusano, K., Suzuki, Y., & Nishikawa, K. 1995, *ApJ*, 441, 942 [21](#)

- Kusano, K., Yokoyama, T., Maeshiro, T., & Sakurai, T. 2003, *Advances in Space Research*, 32, 1931 [21](#)
- LaBonte, B. J., Georgoulis, M. K., & Rust, D. M. 2007, *ApJ*, 671, 955 [4](#)
- Leka, K. D., Canfield, R. C., McClymont, A. N., & van Driel-Gesztelyi, L. 1996, *ApJ*, 462, 547 [10](#)
- Linton, M. G., Dahlburg, R. B., & Antiochos, S. K. 2001, *ApJ*, 553, 905 [21](#)
- Longcope, D. W. 2004, *ApJ*, 612, 1181 [4](#)
- Maurya, R. A., & Ambastha, A. 2009, *Sol. Phys.*, 258, 31 [15](#)
- Maurya, R. A., Vemareddy, P., & Ambastha, A. 2012, *ApJ*, 747, 134 [15](#), [16](#)
- Moon, Y. J., Chae, J., Wang, H., Choe, G. S., & Park, Y. D. 2002, *ApJ*, 580, 528 [3](#), [4](#), [5](#), [21](#)
- Nindos, A., Zhang, J., & Zhang, H. 2003, *ApJ*, 594, 1033 [3](#)
- November, L. J., & Simon, G. W. 1988, *ApJ*, 333, 427 [3](#)
- Pariat, E., Démoulin, P., & Berger, M. A. 2005, *A&A*, 439, 1191 [3](#), [8](#), [17](#), [20](#)
- Park, S.-H., Chae, J., Jing, J., Tan, C., & Wang, H. 2010a, *ApJ*, 720, 1102 [5](#), [21](#)
- Park, S.-h., Chae, J., & Wang, H. 2010b, *ApJ*, 718, 43 [4](#), [23](#), [24](#)
- Petrie, G. J. D., & Sudol, J. J. 2010, *ApJ*, 724, 1218 [15](#)
- Pevtsov, A. A., Canfield, R. C., & Metcalf, T. R. 1995, *ApJ*, 440, L109 [2](#)
- Pevtsov, A. A., Canfield, R. C., Sakurai, T., & Hagino, M. 2008, *ApJ*, 677, 719 [2](#)
- Press, W. H., Teukolsky, S. A., Vetterling, W. T., & Flannery, B. P. 1992, *Numerical recipes in C. The art of scientific computing*, ed. Press, W. H., Teukolsky, S. A., Vetterling, W. T., & Flannery, B. P. [18](#)
- Qiu, J., & Gary, D. E. 2003, *ApJ*, 599, 615 [15](#)
- Romano, P., Pariat, E., Sicari, M., & Zuccarello, F. 2011, *A&A*, 525, A13 [22](#)
- Romano, P., & Zuccarello, F. 2011, *A&A*, 535, A1 [22](#)
- Schou, J., Scherrer, P. H., Bush, R. I., Wachter, R., & et al. 2012, *Sol. Phys.*, 275, 229 [6](#), [8](#)

- Schuck, P. W. 2005, *ApJ*, 632, L53 [4](#)
- . 2006, *ApJ*, 646, 1358 [4](#), [6](#)
- . 2008, *ApJ*, 683, 1134 [4](#), [8](#)
- Sudol, J. J., & Harvey, J. W. 2005, *ApJ*, 635, 647 [15](#)
- Tian, L., Démoulin, P., Alexander, D., & Zhu, C. 2011, *ApJ*, 727, 28 [8](#)
- Tiwari, S. K., Venkatakrishnan, P., Gosain, S., & Joshi, J. 2009, *ApJ*, 700, 199 [2](#)
- Venkatakrishnan, P., & Gary, G. A. 1989, *Sol. Phys.*, 120, 235 [6](#)
- Wang, H., & Liu, C. 2010, *ApJ*, 716, L195 [13](#), [15](#)
- Welsch, B. T., Abbett, W. P., De Rosa, M. L., Fisher, G. H., & et al. 2007, *ApJ*, 670, 1434 [4](#)
- Welsch, B. T., Fisher, G. H., Abbett, W. P., & Regnier, S. 2004, *ApJ*, 610, 1148 [4](#)

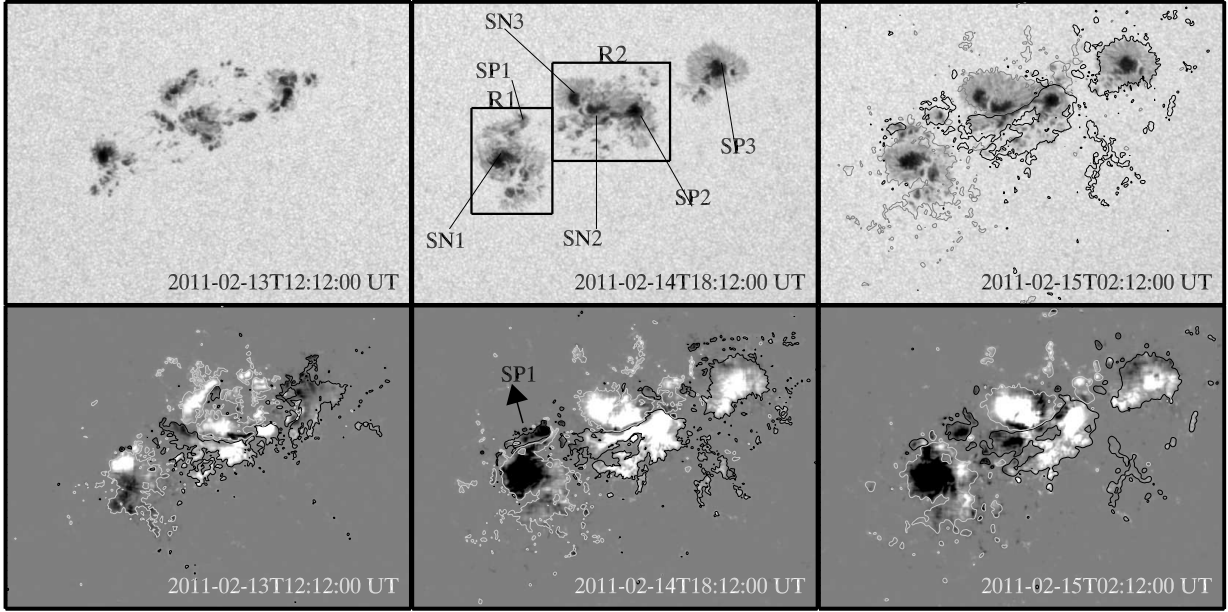


Fig. 1.— (*Top row*) The daily HMI continuum intensity maps of AR NOAA 11158, and (*Bottom row*) the corresponding helicity flux density maps (scaled to $\pm 0.05 \times 10^{20} \text{Mx}^2 \text{cm}^{-2} \text{s}^{-1}$ and also in subsequent plots) computed from Equation 4. The field of view is 275×200 arcsec². The overlaid gray and black contours correspond to LOS magnetic fields at $[-150, 150]$ G levels, respectively. Rectangular boxes in intensity image of 2011 February 14 mark the selected sub-areas R1 and R2 in which velocity flows are shown in the subsequent figures.

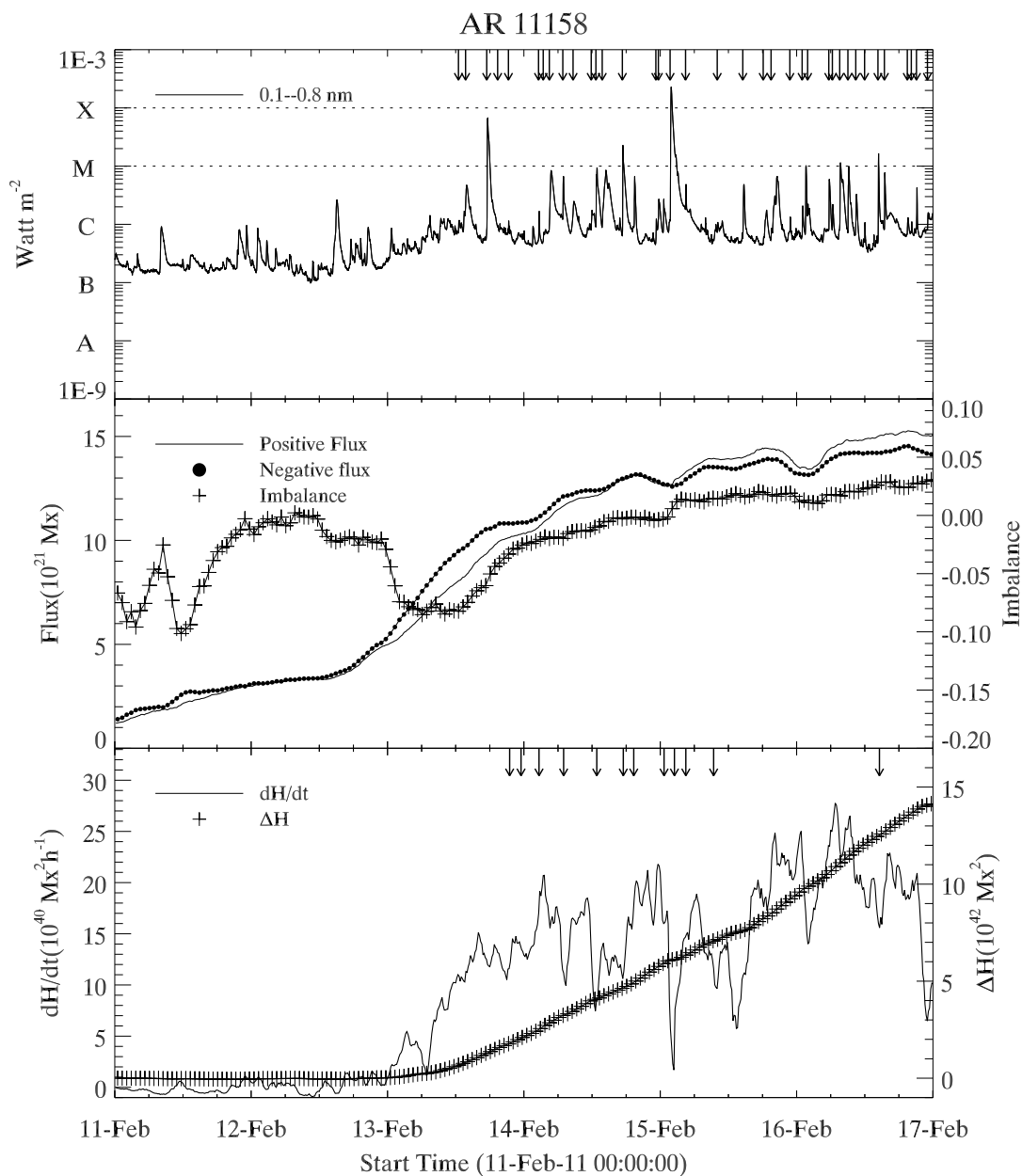


Fig. 2.— *Top*: Solar disk integrated GOES Soft X-ray flux during February 11-16, 2011. The arrows on top panel indicate the start times of flares in AR NOAA 11158. *Middle*: Time profiles of the magnetic fluxes and flux imbalance in the AR. *Bottom*: The computed helicity rates integrated over the whole AR. Arrows in this panel indicate the onset time of CMEs that were launched from this AR.

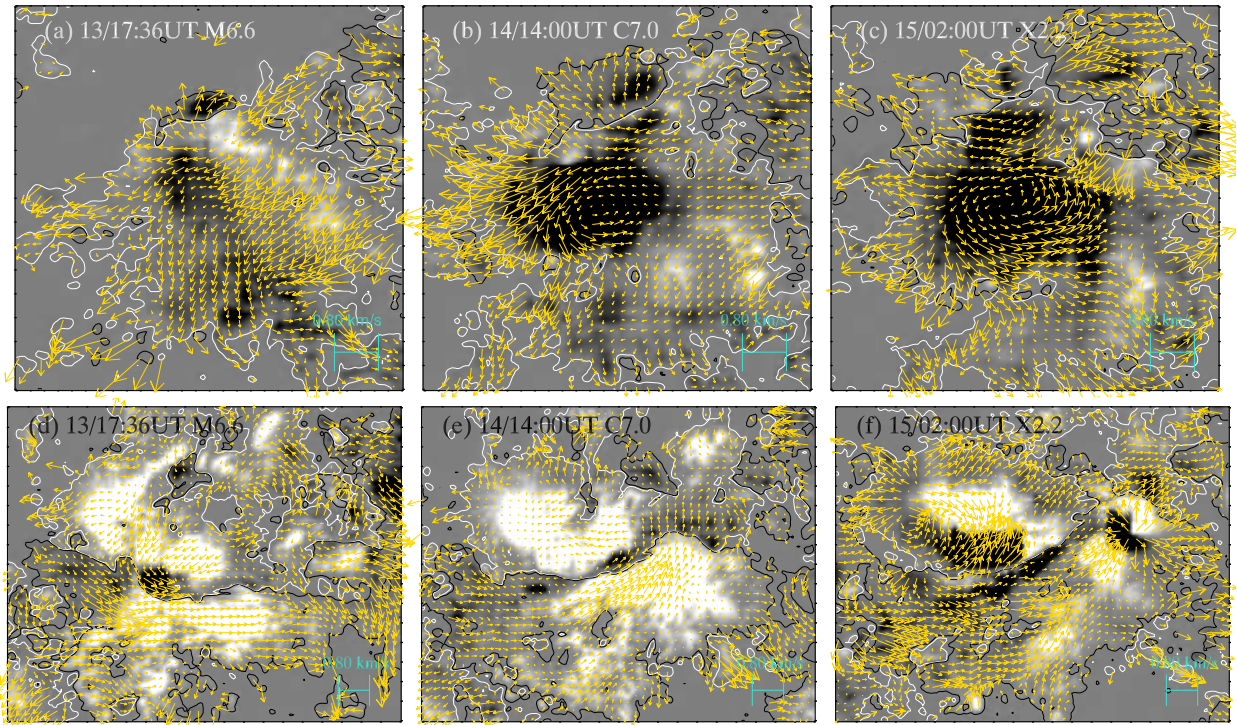


Fig. 3.— Transverse velocity field vectors as inferred from DAVE technique superposed on helicity flux density maps with the LOS magnetic field contours for the rectangular regions of Figure 1 – R1 (*Top row*) and R2 (*Bottom row*). Spiral or vortex like velocity patterns in sunspot penumbra in (b-c) are due to umbral rotation of sunspot SN1. Sites of negative helicity injection are seen around the magnetic polarity inversion line in (d)-(f) at the peak times of the flares noted in each panel.

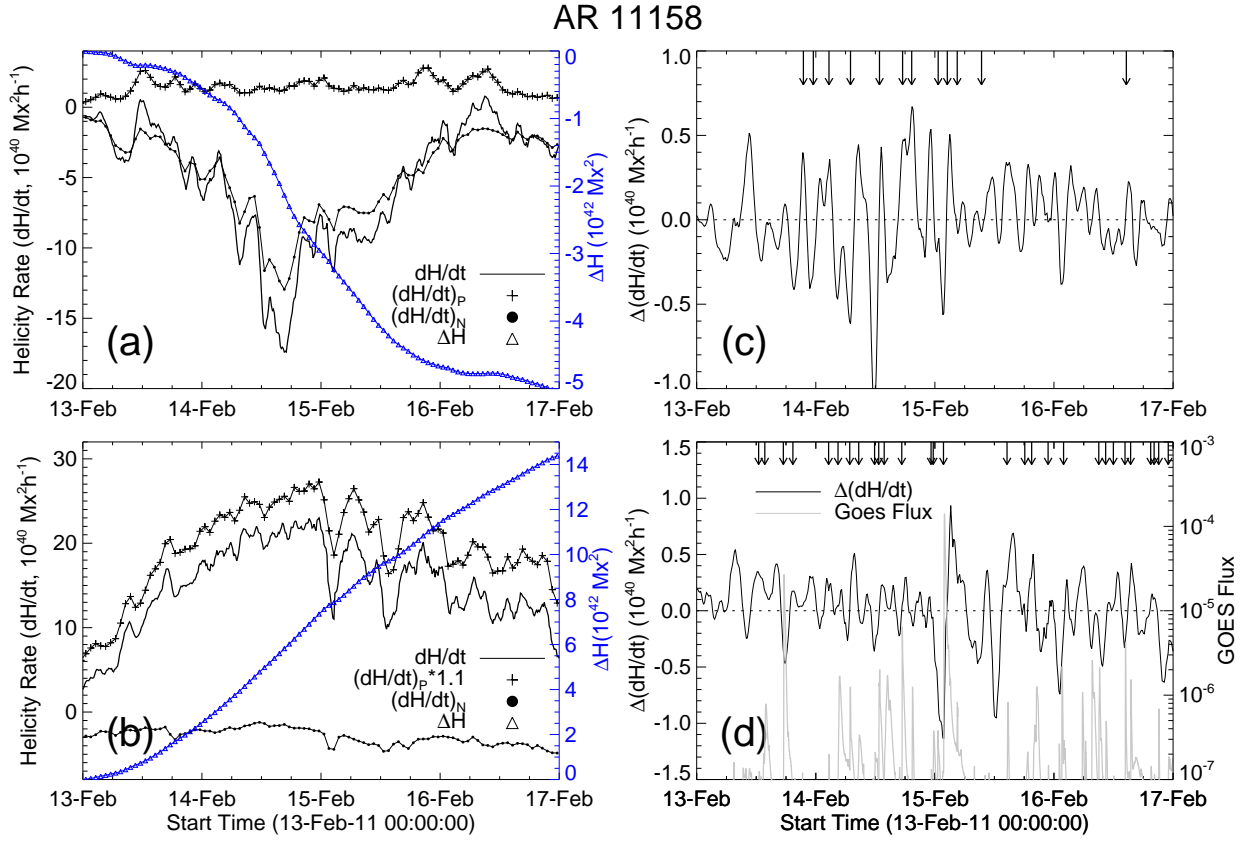


Fig. 4.— Temporal evolution of helicity rate and accumulated helicity integrated over (a) R1 and (b) R2. The time difference of helicity rate ($\Delta(dH/dt)$) in (c) for region R1 with arrows marking CME timings, (d) for region R2 with pointed flares originated from this AR.

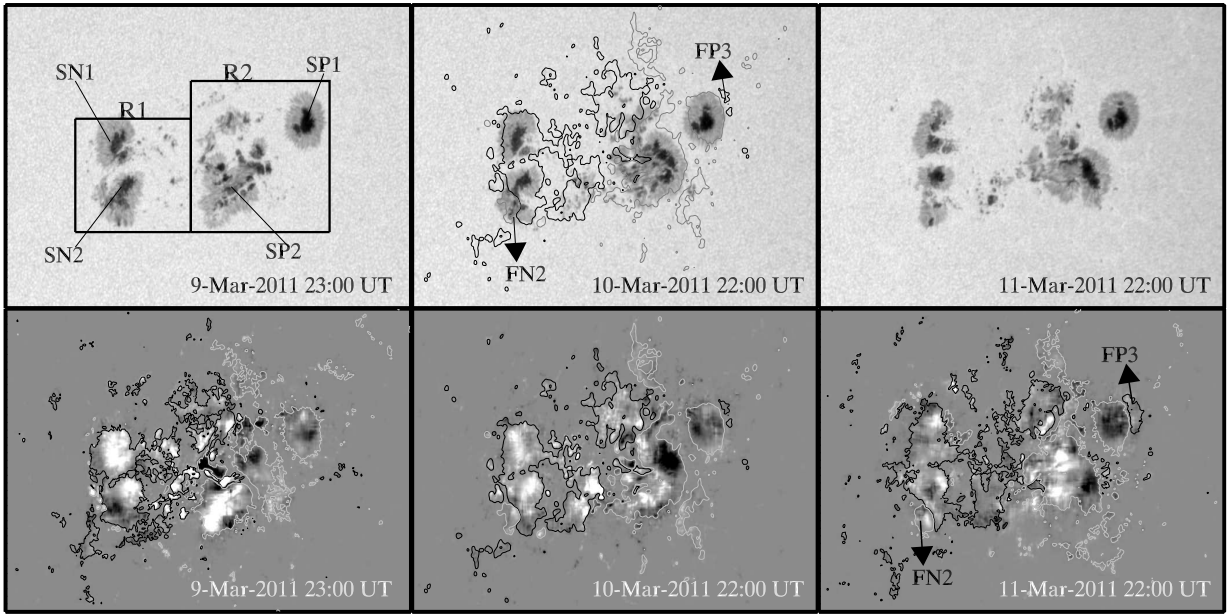


Fig. 5.— (*Top row*) The daily HMI continuum intensity maps of AR NOAA 11166, and (*Bottom row*) the corresponding helicity flux density maps computed from Equation 4. The field of view is 350×200 arcsec². The overlaid gray and black contours correspond to LOS magnetic fields at $[-150, 150]$ G levels, respectively. Rectangular boxes in intensity image of March 9 mark the selected sub-areas in which velocity flows are shown in the next figure. Emerging fluxes from sunspot periphery are indicated as FN2 and FP3 on March 11/22:00UT

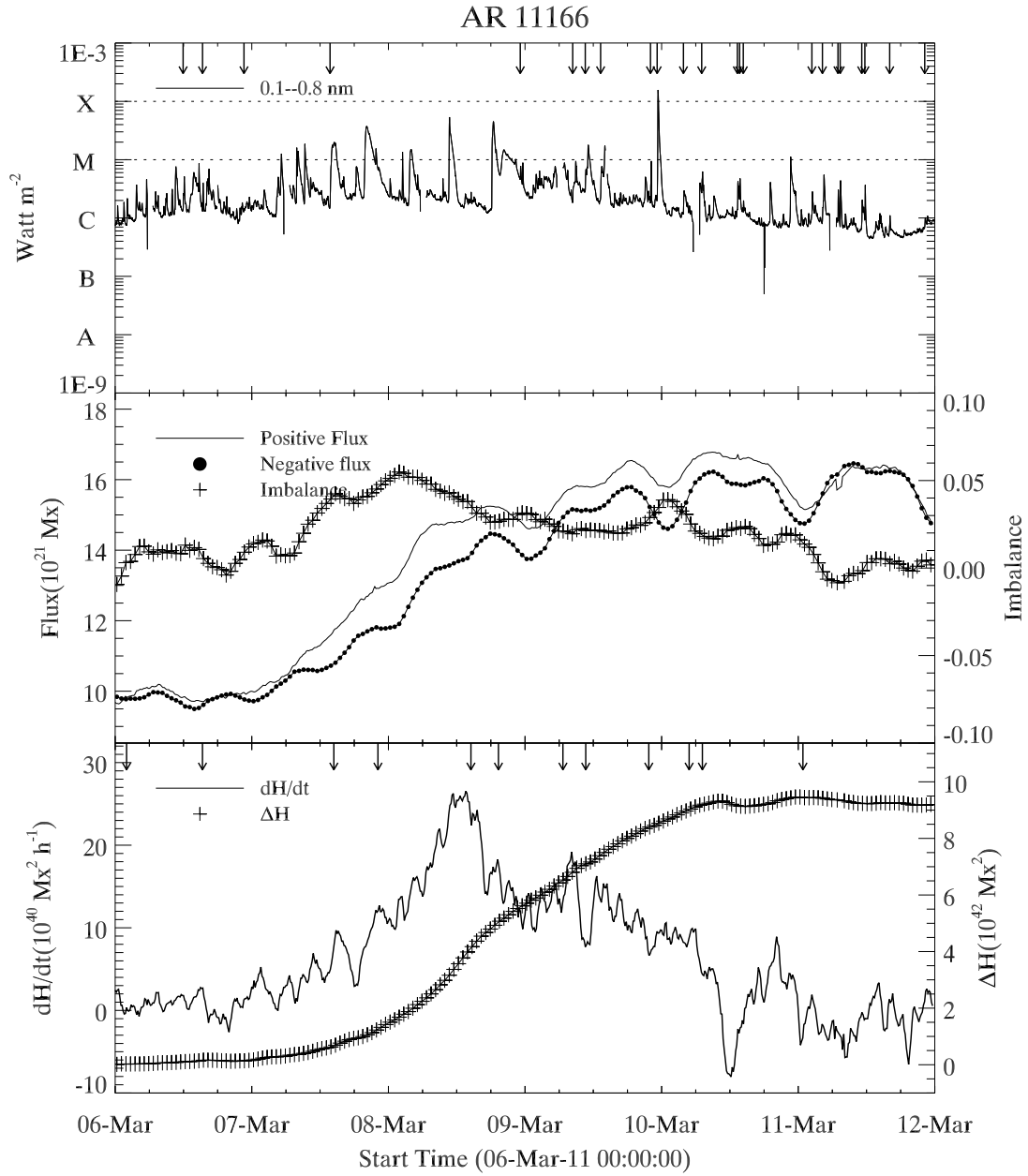


Fig. 6.— Same as Figure 2 but for AR NOAA 11166.

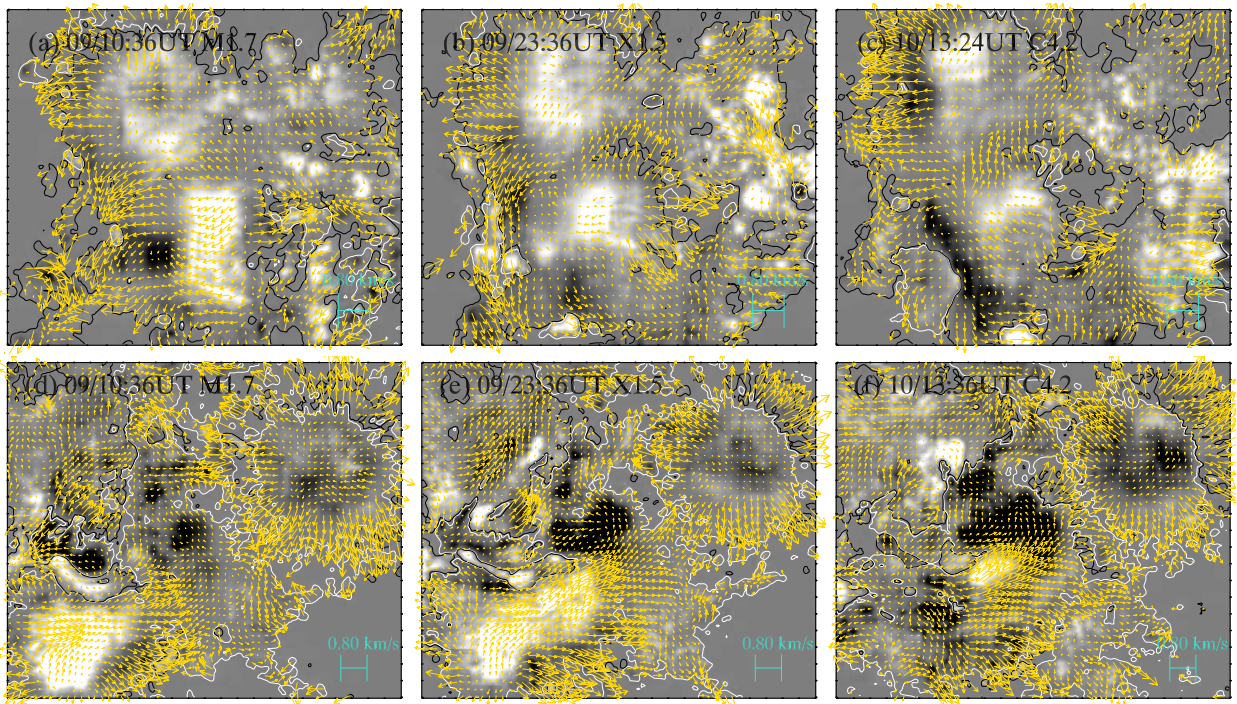


Fig. 7.— Transverse velocity field vectors in the rectangular region R1 (*Top row*) and R2 (*Bottom row*) of Figure 5 overlaid on the helicity flux density maps with iso-contours of LOS magnetic field during flare events.

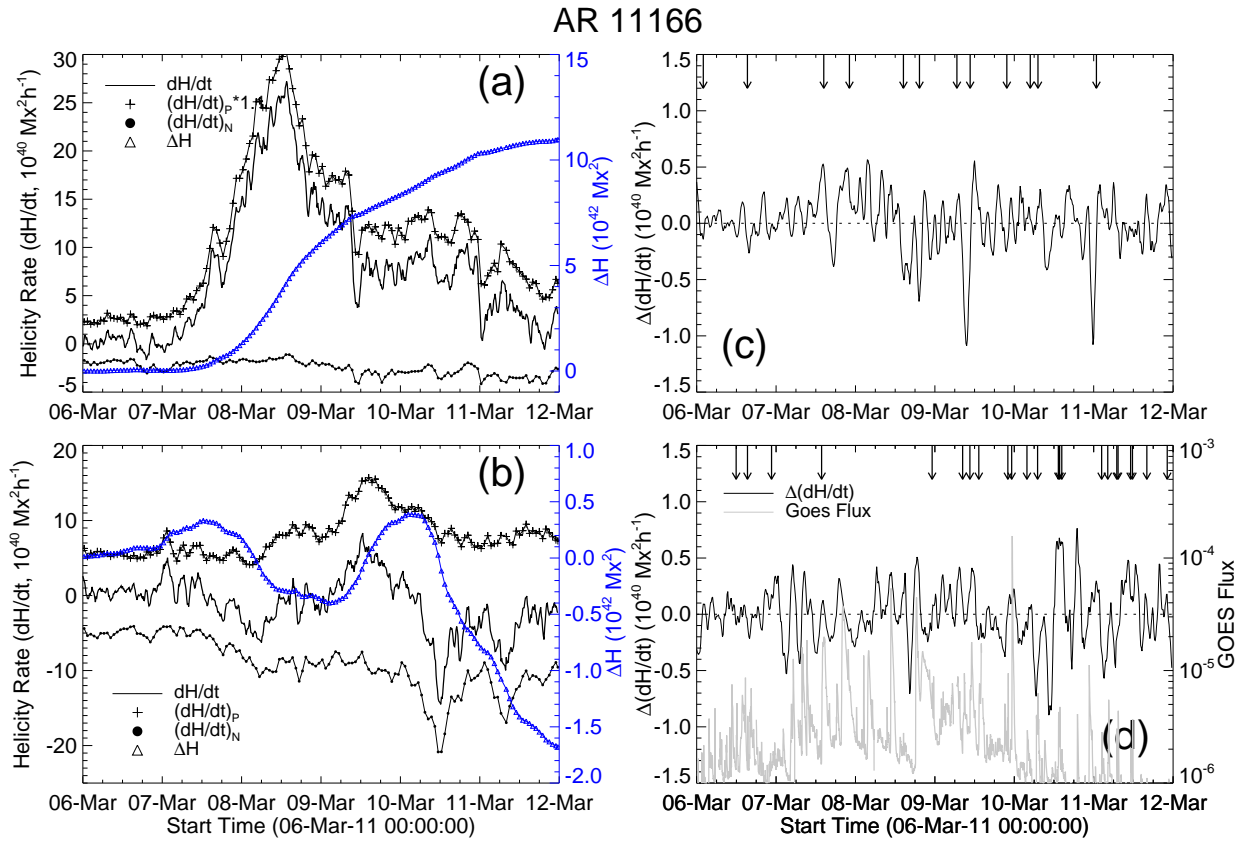


Fig. 8.— Same as Figure 4 but for AR NOAA 11166.

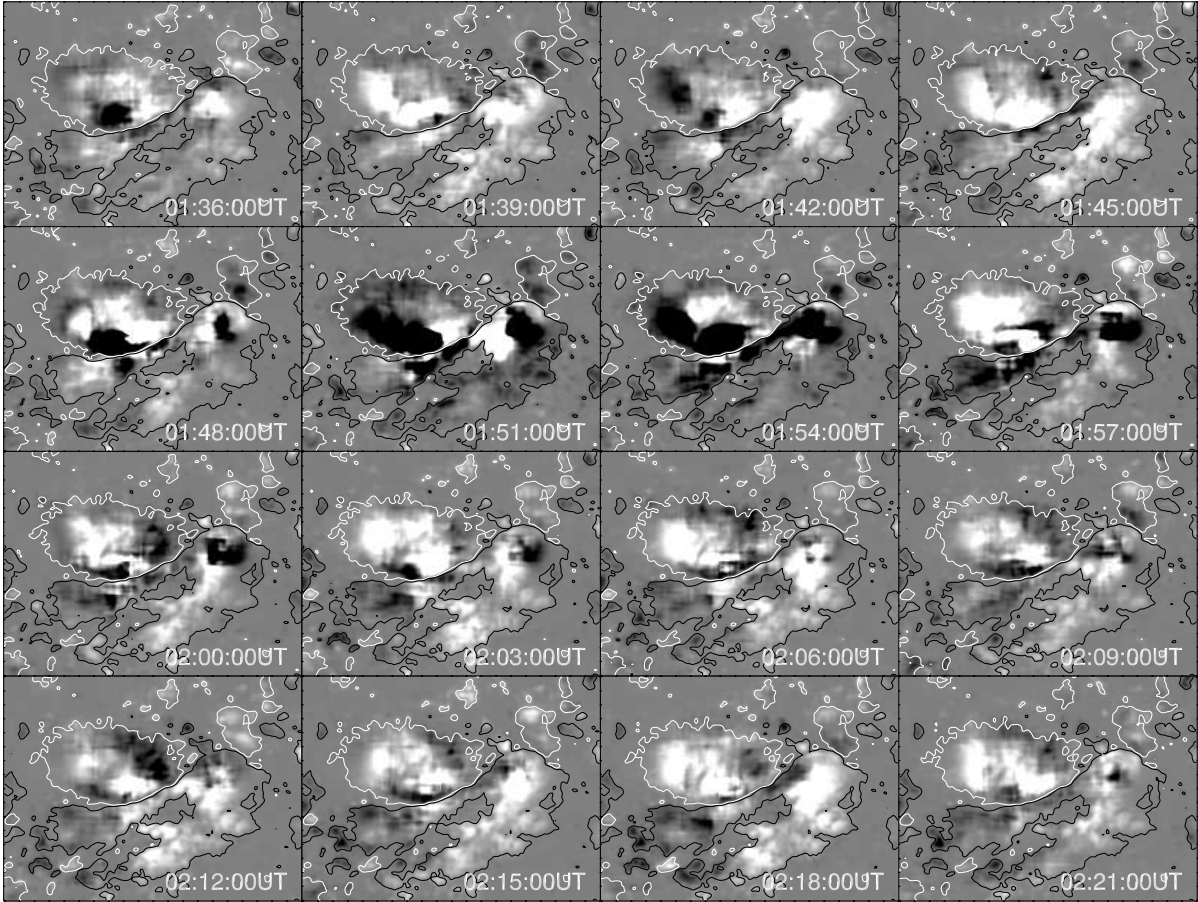


Fig. 9.— Mosaic of injection of helicity flux distribution around the time of X2.2 flare in AR 11158 with iso-contour of LOS positive(negative) flux in black(white). Intense negative helicity flux about the PIL during peak time(01:48–02:00UT) of the flare is evident possibly due to flare-related transient effect on the magnetic field measurements during the impulsive period.

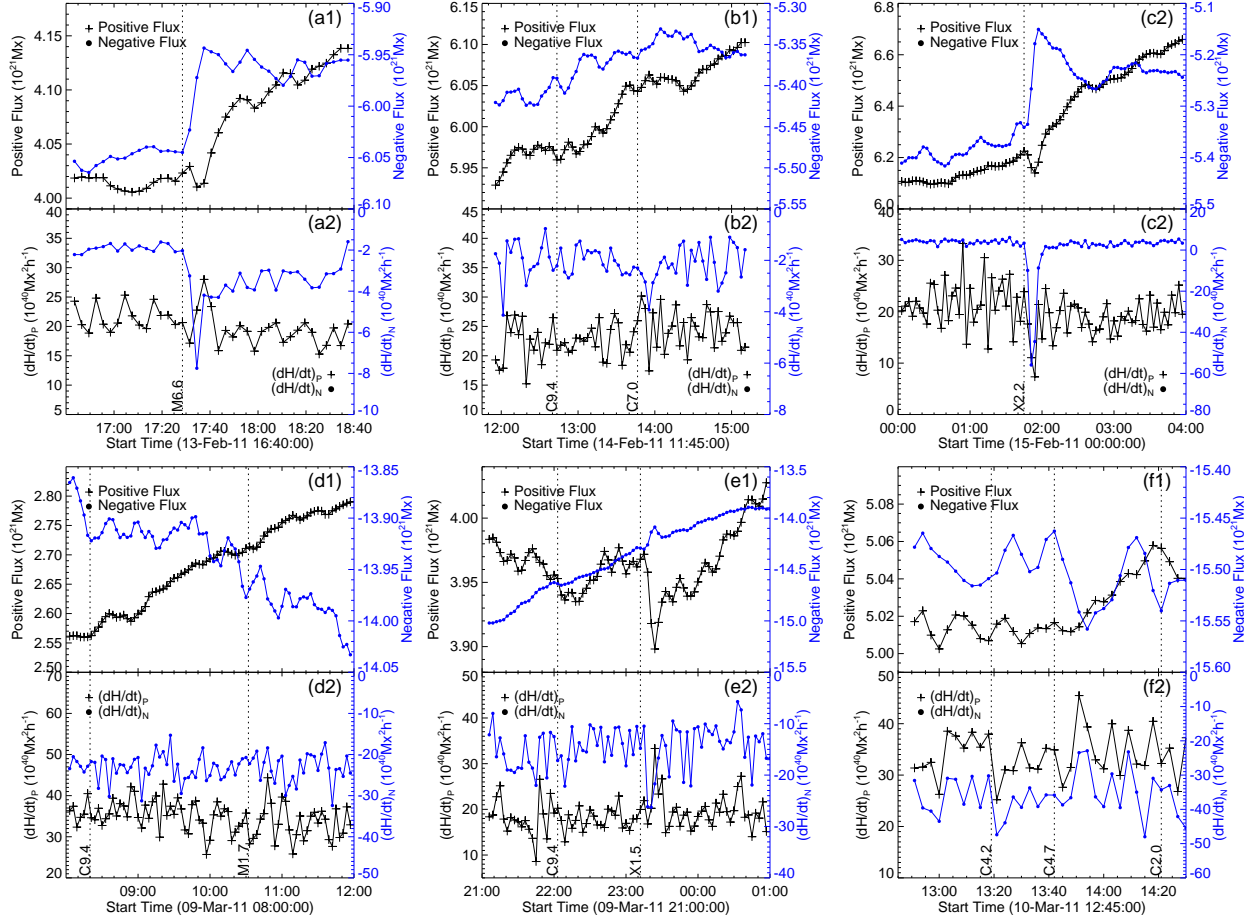


Fig. 10.— Temporal profiles of magnetic and helicity fluxes during some selected flare events in both ARs. Vertical dashed lines indicate onset time of flares as labeled in each panel. See text for more details.

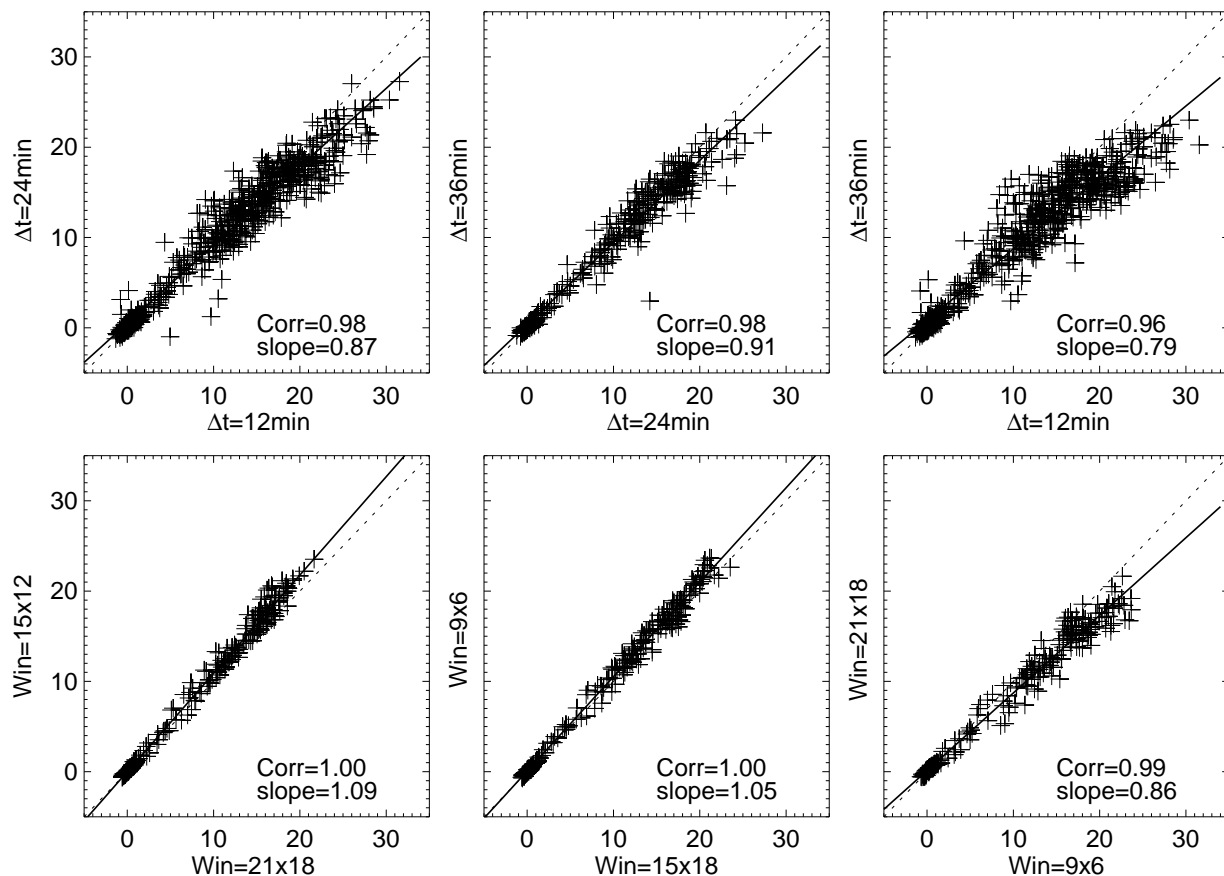


Fig. 11.— Dependence of helicity injection rate (in units of $10^{40} \text{ Mx}^2\text{h}^{-1}$) for AR NOAA 11158 on (*Top row*) the time interval Δt (minutes), and (*bottom row*) the window size(pixel²). The solid line represents the straight line fit to the scattered data points whereas the dotted line indicates slope=1 line for reference. Correlation coefficient and slope of the fitting are noted in each panel.

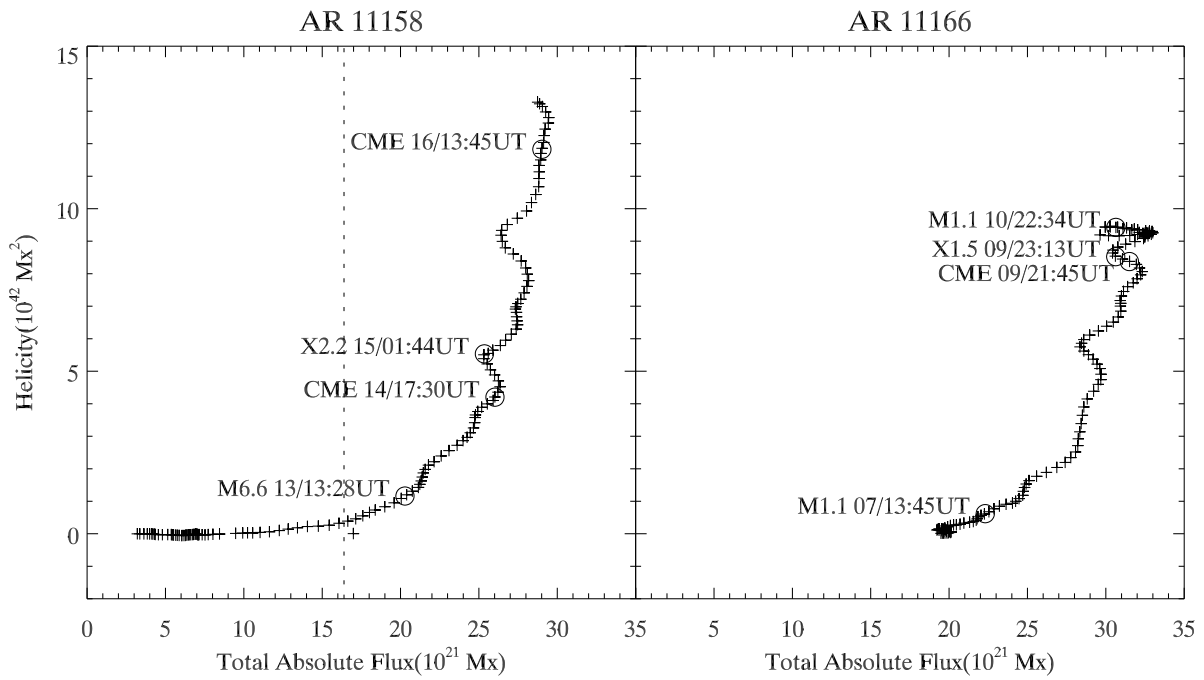


Fig. 12.— Plot of accumulated helicity with total absolute flux computed for NOAA 11158(*Left*) and NOAA 11166(*Right*). The flare/CME events are labeled and shown by circles in each panel.